doi: 10.16539/j.ddgzyckx.2022.01.006

卷(Volume)46, 期(Number)1, 总(SUM)186
页(Pages)112~131, 2022, 2(February, 2022)

大地构造与成矿学
Geotectonica et Metallogenia

峨眉山大火成岩省平川苦橄岩地幔源区性质
——来自橄榄石微量元素的制约

张　磊[1, 2, 3], 任钟元[1, 2*], 张　乐[1, 2]

(1. 中国科学院 广州地球化学研究所, 同位素地球化学国家重点实验室, 广东 广州 510640; 2. 中国科学院深地科学卓越创新中心, 广东 广州 510640; 3. 中国科学院大学, 北京 100049)

摘　要: 橄榄石是基性岩浆中最早期结晶的硅酸盐矿物之一, 其主量、微量元素特征可以反映出岩浆演化环境、岩浆源区岩性和再循环组分性质等重要信息。本次研究通过对峨眉山大火成岩省平川苦橄岩中橄榄石主量和微量元素分析, 以及橄榄石内尖晶石包裹体分析, 并与大理苦橄岩中橄榄石和尖晶石成分进行对比, 来探讨不同苦橄岩母岩浆氧逸度及源区性质的异同。橄榄石-尖晶石-斜方辉石氧逸度计计算结果表明, 平川苦橄岩母岩浆比大理苦橄岩母岩浆具有更高的氧逸度(分别为 ΔQFM+0.24 和 ΔQFM−0.51), 这与平川橄榄石较大理橄榄石具有更高的 V/Sc 值相一致。平川橄榄石具有较高 Ni/Co 值, 暗示苦橄岩源区中存在再循环物质的参与, 橄榄石较低的 Li 含量则进一步表明这种再循环物质更可能是洋壳而不是陆壳物质。在地幔源区判别图中, 平川橄榄石主要位于橄榄岩起源熔体结晶的橄榄石成分区域。然而, 平川橄榄石比大理橄榄石具有更高 Ni、Co 含量和 Zn/Fe、Fe/Mn 值, 低 Ca、Mn、Sc 含量和 Mn/Zn 值, 暗示平川苦橄岩源区中存在辉石岩组分。少量的再循环洋壳与橄榄岩地幔混合, 会形成富橄榄石的混合源区, 且这种地幔产生的熔体结晶的橄榄石与平川橄榄石一样, 成分仍近似于橄榄岩熔体中结晶的橄榄石。但平川橄榄石主量、微量元素特征表明, 其成分受源区中辉石岩组分的控制, 结合平川橄榄石较大的成分变化范围, 进一步表明平川苦橄岩地幔源区中是含有辉石岩组分的, 而不是均一的橄榄岩源区。

关键词: 峨眉山大火成岩省; 苦橄岩; 橄榄石; 辉石岩; 氧逸度

中图分类号: P584; P595　　**文献标志码:** A　　**文章编号:** 1001-1552(2022)01-0112-020

0　引　言

大火成岩省(LIP)代表了地球历史上短时间存在的大规模岩浆事件(Coffin and Eldholm, 1992; Bryan and Ernst, 2008), 这些事件产生了巨量的基性火山岩和相应的侵入体, 广泛分布在现今大陆和大洋盆地之上。许多 LIP 被认为与地幔柱有关, 因此对研究地球地幔性质具重要意义。峨眉山大火成岩省位于扬子板块西缘, 是我国境内典型的 LIP 之一(Chung and Jahn, 1995; 图 1)。已有研究表明峨眉山 LIP 形成与地幔柱活动有关, 且可能是导致瓜德普鲁统生物灭绝的因素之一(Zhang et al., 2013; Yang et al., 2015)。峨眉山 LIP 的岩性以基性岩为主, 伴有少量中-酸性岩(Xu et al., 2001, 2010)。这些基性岩绝大多数为拉斑玄武岩, 较演化(MgO<8%), 并普遍遭受了强烈的蚀变作用(Li et al., 2010; Ren et al., 2017)。在地球化学组成上, Xu et al. (2001)提出以 Ti/Y=500 为界, 把峨眉山大火成岩省中基性岩分为高钛和低

收稿日期: 2020-12-04; **改回日期:** 2021-03-09

项目资助: 中国科学院战略性先导科技专项(B 类)(XDB18000000)资助。

第一作者简介: 张磊(1992–), 男, 博士研究生, 矿物学、岩石学、矿床学专业。E-mail: zhanglei415@mails.ucas.edu.cn

通信作者: 任钟元(1962–), 男, 研究员, 从事岩石学和地球化学方向研究。E-mail: zyren@gig.ac.cn

钛两类玄武岩。随着研究的不断深入, 人们逐渐发现峨眉山玄武岩 Ti/Y 值是连续变化的(Kamenetsky et al., 2012; Ren et al., 2017)。

对于峨眉山大火成岩省高钛−低钛岩浆的成因以及地幔源区性质, 一直是地学界研究的热点问题。一些研究者认为, 高钛岩浆与地幔柱直接相关, 而低钛岩浆则来源于大陆岩石圈地幔的高程度熔融, 或受到地壳物质的明显混染(Xu et al., 2001; Xiao et al., 2004; Wang et al., 2007; Fan et al., 2008; Zhou et al., 2008)。Xu et al. (2007)通过 Re-Os 同位素研究认为, 低钛玄武岩来源于地幔柱源区, 而高钛玄武岩来源于大陆岩石圈地幔, 或是地幔柱有关的岩浆在上升过程中有大量岩石圈地幔物质的混染; Shellnutt and Jahn (2011)提出, 高钛和低钛玄武质岩浆可能来源于相同的源区, 它们的成分差异可能是由于部分熔融程度不同和地壳混染造成的; Hou et al. (2011)认为岩浆中 Ti/Y 值差异并不是源区不同造成的, 而主要是受控于铁钛氧化物的分离结晶。岩浆源区性质方面, 前人普遍认为峨眉山玄武岩的源区以橄榄岩为主(Xu et al., 2001; Xiao et al., 2004; Zhang et al., 2006; Lai et al., 2012; Huang et al., 2014)。随着研究的深入, 一些学者认为辉石岩可能存在于峨眉山玄武岩源区(Kamenetsky et al., 2012; Ren et al., 2017; Liu et al., 2017; Yu et al., 2017)。Kamenetsky et al. (2012)提出高钛岩浆来源于辉石岩源区, 低钛岩浆来源于橄榄岩源区; Ren et al. (2017)根据峨眉山苦橄岩中的橄榄石成分, 以及大理苦橄岩较均一的熔体包裹体 Pb 同位素特征, 认为高钛岩浆和低钛岩浆均来源于较均一的辉石岩源区。

橄榄石是基性岩浆中早期结晶的硅酸盐矿物。橄榄石微量元素(如 Ni、Ca、Fe、Mn 等)广泛用于区分不同的地幔源区组分(Ren et al., 2017; Liu et al., 2017; Yu et al., 2017; Yao et al., 2019; Xu et al., 2020)。在组成上地幔的矿物中, Ni 主要存在于橄榄石中, Ca、Mn 主要存在于辉石和石榴子石中, 且只有橄榄石的 $D_{Fe/Mn}$>1(Humayun et al., 2004)。因此, 辉石岩源区起源的熔体被认为比橄榄岩源区熔体具更高 Ni 含量和 Fe/Mn 值, 以及低 Ca、Mn 含量, 这种特征也同样会反映在这些熔体结晶的橄榄石中(Sobolev et al., 2005, 2007; Herzberg, 2011)。不过也有学者提出, 这些判断指标并不是绝对的, 主要由于橄榄石中微量元素含量和比值会受源区成分、形成时温压条件以及熔体成分影响(Yang et al., 2016; Heinonen and Fusswinkel, 2017; Matzen et al., 2017)。Matzen et al. (2017)指出, 橄榄岩源区在不同压力下部分熔融对 Ni 和 Mn 的分配有很强影响。Heinonen and Fusswinkel (2017)提出 Karoo 大火成岩省麦美奇岩中橄榄石的高 Ni、低 Mn 特征是由于深部较高温压的熔融条件所导致, 因此不需要引入辉石岩组分来解释镁铁−超镁铁质岩石中富 Ni 和贫 Mn 橄榄石的成分特征。在峨眉山大火成岩省研究中, Yao et al. (2019)指出峨眉山苦橄岩中橄榄石的 Mn/Zn 、10000×Zn/Fe 值与橄榄岩源区熔体中结晶的橄榄石成分一致; Xu et al. (2020)提出结晶/熔融压力变化可用于解释峨眉山大火成岩省苦橄岩中橄榄石的成分范围, 并认为峨眉山大火成岩省的源区中没有辉石岩组分的参与; Yao et al. (2019)和 Xu et al. (2020)均发现在 Ni-Mn/Zn 和 100×Mn/Fe-10000×Zn/Fe 图解中, 峨眉山大火成岩省样品主要落在橄榄岩区域。因此, 峨眉山大火成岩省源区中是否含有辉石岩至今仍然存在争议。

橄榄石中的第一排过渡元素(FRTE)(如 Sc、Zn、Co)特征可反映源区岩性信息(Le Roux et al., 2010, 2011; Davis et al., 2013; Foley et al., 2013; Søager et al., 2015), 通过对橄榄石成分研究也可以获得岩浆氧逸度、橄榄石结晶温度和岩浆中 H_2O 含量等信息(Ballhaus et al., 1991; Wan et al., 2008; Mallmann and O'Neill, 2013; Coogan et al., 2014; Gavrilenko et al., 2016; Nikolaev et al., 2016)。峨眉山苦橄岩中, 普遍存在高 Fo 橄榄石(比如本研究中的平川苦橄岩中的橄榄石 Fo 可达 91.6), 表明其是从原始的岩浆结晶而来。本文以平川苦橄岩中的橄榄石为研究对象, 选取含有尖晶石包裹体的橄榄石, 进行橄榄石主、微量元素以及尖晶石的主量元素成分分析, 从而估算平川苦橄岩的岩浆氧逸度, 讨论橄榄石成分特征与源区矿物组成以及与再循环物质之间的关系, 希望对峨眉山大火成岩省源区组成及性质有所启示。

1　地质背景与样品介绍

峨眉山大火成岩省位于扬子板块西缘, 在越南、中国西藏羌塘地区和广西西部也有少量峨眉山玄武岩及苦橄岩分布(Chung et al., 1998; Hanski et al., 2004; Wang et al., 2007; Fan et al., 2008; Anh et al., 2011; Liu et al., 2016), 大火成岩省西南部在新生代印度板块和亚欧板块的碰撞中被侵蚀(Ali et al., 2004; Zhou et al., 2006)。峨眉山大火成岩省分布面积大于 2.5×10^5 km^2。喷出岩岩性由亚碱性及偏碱性

的基性火山熔岩及火山碎屑岩组成, 多为无斑隐晶质; 酸性岩主要为流纹岩和花岗岩, 主要与岩浆活动晚期的玄武岩共存(Xu et al., 2010); 苦橄岩较少, 呈小露头发现于丽江、大理、宾川、永胜、平川、松达、玉门等地(Zhang et al., 2006, 2008; Wang et al., 2007; Hanski et al., 2010; Kamenetsky et al., 2012; Tao et al., 2015; Ren et al., 2017; Yu et al., 2017, 2020; Wu et al., 2018; Yao et al., 2019)。峨眉山大火成岩省中产有钒钛磁铁矿(如攀枝花、红格、白马、新街)和铜镍硫化物矿床(如金宝山、力马河、朱布)(Wang et al., 2005, 2007, 2008, 2010; Tao et al., 2007, 2008, 2010; Hou et al., 2012; Tang et al., 2013; Song et al., 2013; Wang and Zhou, 2013; 宋谢炎等, 2018; Bai et al., 2019; Cao et al., 2019), 其中钒钛磁铁矿矿床赋存于多个镁铁质-超镁铁质层状岩体中, 组成了攀西地区超大型 Fe-Ti 氧化物矿集区(王焰等, 2017)。峨眉山大火成岩省岩浆事件的主喷发阶段在 260 Ma (Zhong et al., 2014, 2020; Li et al., 2017), 喷发持续时间至少为 6 Ma(Shellnutt et al., 2020), 这些火山喷发可能导致了瓜德普鲁期生物大灭绝(Wignall et al., 2009; Zhang et al., 2013; Yang et al., 2015; Xu et al., 2018)。根据峨眉山玄武岩下伏茅口组灰岩的剥蚀程度差异, 峨眉山大火成岩省可划分为内带、中带、外带三个区域(图 1)(He et al., 2003; Xu et al., 2004)。

本次研究样品采自四川省盐源县平川铁矿区, 位于峨眉山大火成岩省内带北缘。矿区内可见苦橄质岩脉呈岩墙产出, 厚度约 10 m, 岩脉侵入到二叠系茅口组灰岩中, 且与围岩接触界线清晰。苦橄岩样品呈斑状结构, 斑晶主要由橄榄石(30%~40%)以及极少量(<5%)单斜辉石组成。橄榄石斑晶多呈自形-它形产出, 粒度多介于 0.5~3 mm 之间, 沿裂隙和边部发生蛇纹石化和绿泥石化, 剩下橄榄石残晶(图 3); 橄榄石中多包裹有自型尖晶石, 其粒度通常小于 20 μm。基质主要由细粒的橄榄石、单斜辉石、斜长石以及 Fe-Ti 氧化物组成。平川苦橄岩具有较高 MgO 含量(17.6%~24.8%), 较低 CaO(8.0%~9.6%)和 Al_2O_3(8.0%~9.6%)含量, 属于拉斑玄武岩; 全岩 Ti/Y=472~507(吴亚东, 2018)。大理苦橄岩(全岩 Ti/Y=358~408)是峨眉山大火成岩省中研究程度较高的苦橄岩(Zhang et al., 2013, 2019a; Ren et al., 2017; Wu et al., 2018; 张乐, 2019), 本次也对大理苦橄岩的橄榄石及尖晶石包裹体进行分析, 并与平川橄榄石进行对比。

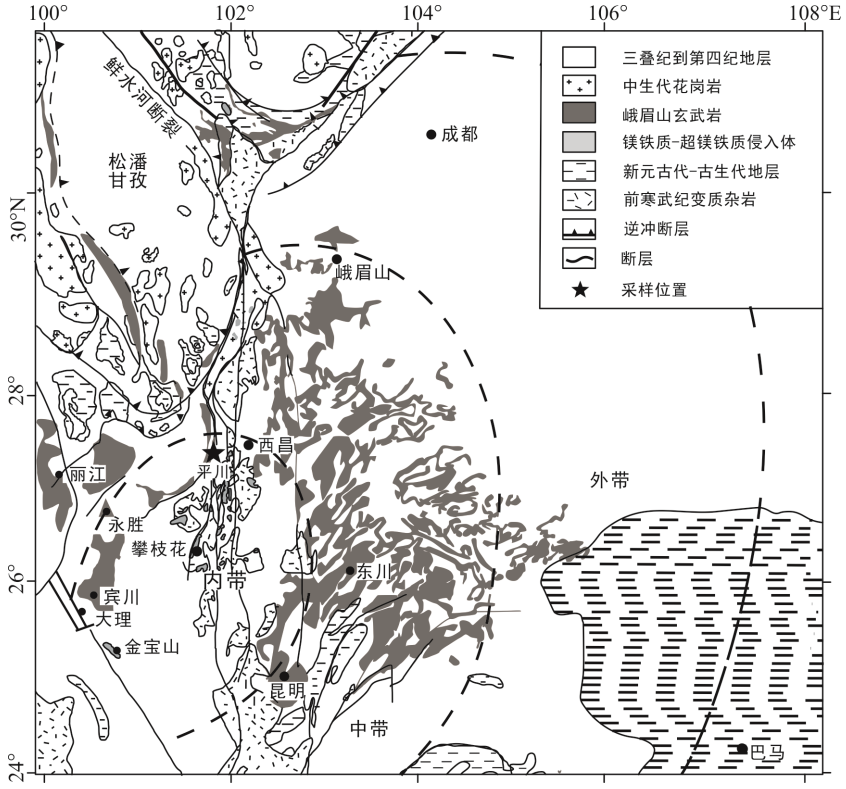

图 1　峨眉山大火成岩省玄武岩和镁铁质-超镁铁质侵入体分布图(据 Kamenetsky et al., 2012 修改)

Fig.1　Geological map of the basalts and mafic-ultramafic intrusions in the Emeishan large igneous province

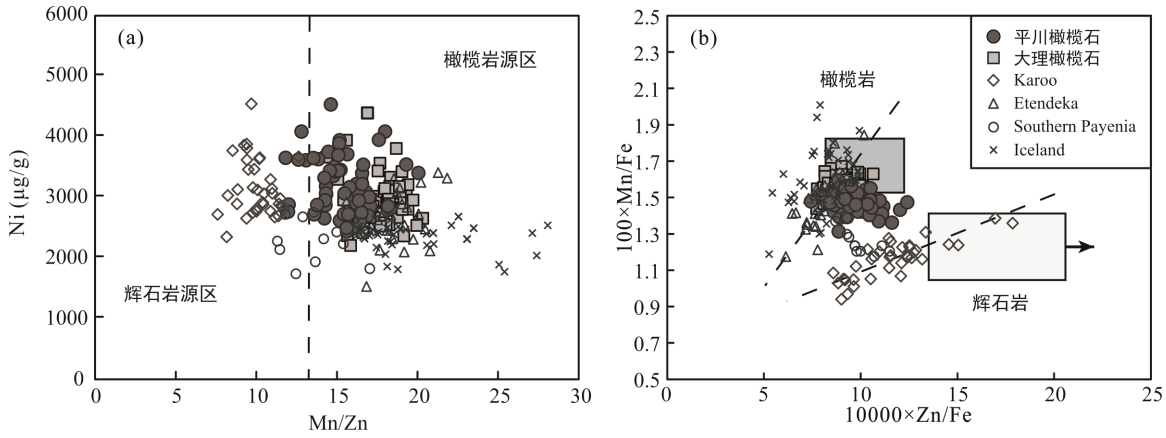

Karoo 苦橄岩中的橄榄石来自具有高比例壳源再循环物质的无橄榄石辉石岩地幔源区(Harris et al., 2015; Kamenetsky et al., 2017, Howarth and Harris, 2017); Etendeka 苦橄岩中的橄榄石来自于橄榄岩源区(Thompson et al., 2001, Howarth and Harris, 2017); Southern Payenia 玄武岩中的橄榄石代表橄榄岩−辉石岩混合源区熔体中产生的橄榄石(Søager et al. 2015, Howarth and Harris, 2017); Iceland 橄榄石来自于含有约 10%辉石岩的地幔源区(Shorttle et al., 2014, Neave et al., 2018)。数据来源: Karoo 苦橄岩和 Etendeka 苦橄岩中橄榄石据 Howarth and Harris (2017); Southern Payenia 橄榄石据 Søager et al. (2015); Iceland 橄榄石据 Neave et al. (2018)。

图 2　橄榄石 Ni-Mn/Zn(a)和 100×Mn/Fe-10000×Zn/Fe(b)地幔源区判别图(据 Howarth and Harris, 2017)

Fig.2　Plots of Ni *vs.* Mn/Zn (a) and 100×Mn/Fe *vs.* 10000×Zn/Fe (b) for the olivines

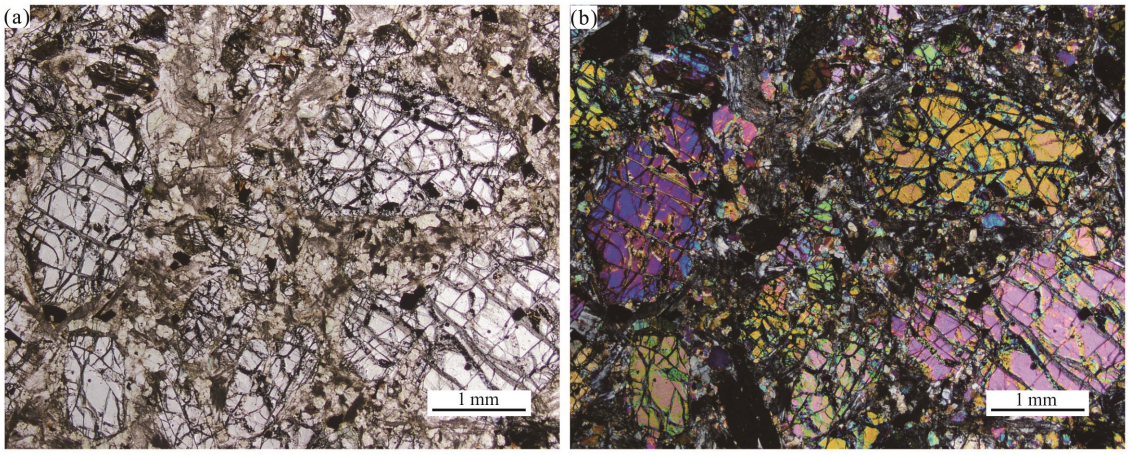

图 3　典型的平川苦橄岩显微镜下照片

Fig.3　Typical microscopic photographs of the Pingchuan picrites

2　分析方法

首先切除样品的风化表面, 将样品破碎成 1 cm 大小的小块, 之后使用 SELFRAG 高压脉冲破碎仪对样品进行进一步的破碎。该仪器可以使样品尽可能沿着颗粒边界裂解开, 从而保持矿物颗粒的相对完整。使用双目显微镜从粉碎的矿物颗粒中手工挑取新鲜的橄榄石颗粒, 将挑取的橄榄石镶嵌在环氧树脂中, 仔细抛光使包裹在橄榄石中的尖晶石暴露至靶表面用于后续分析(Ren et al., 2005, 2017)。所有分析均在中国科学院广州地球化学研究所同位素地球化学国家重点实验室进行。

橄榄石的主量元素分析在 JEOL JXA-8210 上进行。测试条件为: 加速电压 15 kV, 电流 20 nA, 束斑直径 3 μm。重复分析橄榄石标样 MongOL(Batanova et al., 2019)显示, SiO_2、MgO 和 FeO 的分析精度(2RSD)均优于 1.4%。尖晶石的主量元素分析在 Cameca SXFiveFE 场发射电子探针上完成, 具体条件为: 加速电压 20 kV, 电流 20 nA, 束斑直径 2 μm。每测试 5 个点测试一次 Chromite-1 玻璃标样, 其中 Cr_2O_3、Al_2O_3 和 MgO 的分析精度(2RSD)优于 1%, FeO、TiO_2 的分析精度(2RSD)优于 2.4%。

采用激光剥蚀高分辨扇形磁场电感耦合等离子体

质谱仪(LA-SF-ICP-MS)进行橄榄石微量元素分析(表 1)。配有 193 nm 准分子激光器(COMPexPro)的激光剥蚀系统(RESOlution M-50)用于原位烧蚀样品, 分析使用的激光直径为 45 μm, 频率 6 Hz, 能量密度为约 4 J/cm^2。氦气被用作载气, 将剥蚀产生的气溶胶运载到质谱中。测试使用的质谱仪为 Thermo Fisher Scientific 的 ELEMENT XR 电感耦合等离子质谱仪, 该仪器的灵敏度高于传统四级杆 ICP-MS, 并可以在低、中、高质量分辨率模式下工作。该检测器由一个二次电子倍增器和一个法拉第杯组成, 可提供从 0 到 10^{12} 次计数/秒(cps)的线性动态范围。质谱的接口部分采用标准的 Ni 采样锥和 Ni 截取锥, 相比 X 截取锥和 Jet 样品锥可以降低分子氧化物的产率。在测试每个样品前, 激光剥蚀 3 下来清除样品表面可能的污染。每测试一个点包括 20 s 的背景采集和 30 s 的激光剥蚀。在分析过程中使用 USGS 标样 BCR-2G、BHVO-2G 和 GSD-1G 作为校正标样, 使用 TB-1G 作为监控标样。TB-1G 的测试结果显示大部分元素的测试误差(2RSD)小于 10%。详细的实验过程见 Zhang et al. (2019b)。

表 1　平川苦橄岩中橄榄石的主量元素和微量元素组成

Table 1　Chemical compositions of olivine phenocrysts from the Pingchuan picrites

样品	PCTK-3-3	PCTK-3-4	PCTK-3-5	PCTK-3-6	PCTK-3-8	PCTK-3-9	PCTK-3-10	PCTK-3-12	PCTK-3-13	PCTK-4-1	PCTK-4-2	PCTK-4-3	PCTK-4-4
SiO_2	40.02	40.43	40.04	40.17	39.90	40.32	40.83	39.71	40.02	39.80	41.15	39.67	40.19
FeO	14.80	14.18	14.38	14.81	14.20	14.05	10.94	16.38	14.36	13.74	8.74	14.67	11.98
MgO	44.80	45.27	45.36	45.50	45.94	45.72	48.13	43.85	44.76	44.76	49.35	44.66	46.81
Fo	84.37	85.06	84.90	84.56	85.22	85.30	88.69	82.67	84.74	85.30	90.96	84.44	87.44
Ni	2778	2976	2990	2882	2892	2673	3204	2604	2844	3169	3739	3037	3418
Li	1.91	1.73	1.62	0.989	1.84	1.79	1.18	1.63	1.85	1.50	1.37	1.47	0.654
Na	54.8	37.3	41.8	40.7	41.7	40.6	49.5	37.8	41.6	31.0	32.5	33.1	36.4
Al	267	319	227	268	317	218	400.	306	280	304	355	239	331
P	40.2	32.1	31.2	23.3	32.1	57.9	29.0	25.2	67.2	46.4	99.7	42.2	37.1
Ca	2946	2736	2890	2663	2667	3029	2555	2683	2809	2372	2395	2665	2435
Sc	9.13	9.32	8.44	8.53	8.93	8.42	7.00	9.65	9.50	8.33	6.12	8.46	7.20
Ti	74.1	84.3	54.4	114.0	85.6	75.3	68.1	88.0	67.7	55.2	40.3	96.0	49.8
V	9.36	7.99	6.89	7.43	8.90	7.90	8.03	10.1	9.06	7.99	6.36	6.91	6.28
Cr	308	418	360	277	362	386	739	293	352	467	657	259	581
Mn	1988	1894	1827	1876	1769	1776	1376	2107	1893	1695	1074	1827	1425
Co	195	197	190	197	189	196	202	203	197	187	173	190	188
Cu	6.03	11.4	8.50	8.02	9.00	7.50	5.99	12.1	8.24	9.89	6.76	9.33	6.43
Zn	110	117	1010	115	110	107	85.3	140	111	119	74.6	128	95.5
Ga	48.0	49.0	45.4	33.1	56.3	55.3	63.2	66.6	55.1	55.5	75.9	53.2	52.5
Y	197	146	96.3	155	210	79.6	144	224	109	188	125	161	128
Zr	97.9	81.3	8.50	123	75.9	88.1		103	34.9	46.0	91.5	118	57.7

样品	PCTK-4-5	PCTK-4-6	PCTK-4-7	PCTK-4-8	PCTK-4-9	PCTK-4-10	PCTK-7-3	PCTK-7-4	PCTK-7-5	PCTK-7-7	PCTK-7-8	PCTK-7-10	PCTK-7-11
SiO_2	39.24	40.07	40.30	40.44	39.61	39.98	39.36	41.56	39.09	39.79	41.44	40.01	40.25
FeO	15.53	12.19	9.72	10.13	14.95	11.45	15.98	9.08	16.28	14.25	9.29	12.07	13.03
MgO	42.65	46.62	47.84	47.60	44.16	46.35	43.60	50.07	43.24	44.61	50.33	46.56	46.14
Fo	83.03	87.21	89.76	89.33	84.03	87.83	82.95	90.76	82.56	84.80	90.62	87.31	86.33
Ni	2869	3598	4072	3441	2639	3491	2711	3930	2752	2803	3876	3078	2842
Li	1.19	1.81	0.902	1.70	1.49	1.19	2.34	0.909	1.05	1.56	0.378		0.574
Na	21.6	26.9	30.6	36.4	31.2	39.0	39.2	31.2	31.9	34.7	59.8	41.1	37.6
Al	221	323	330	286	255	249	221	305	193	423	333	280	258
P	77.9	56.8	25.1	48.0	46.5	50.6	36.7	27.7	28.4	28.1	29.2	19.0	26.4

续表 1:

样品	PCTK-4-5	PCTK-4-6	PCTK-4-7	PCTK-4-8	PCTK-4-9	PCTK-4-10	PCTK-7-3	PCTK-7-4	PCTK-7-5	PCTK-7-7	PCTK-7-8	PCTK-7-10	PCTK-7-11
Ca	2668	2281	2099	2401	2719	2507	2544	2105	2802	3487	2239	2549	2724
Sc	7.70	6.43	5.45	6.37	9.53	6.42	8.31	6.16	7.42	11.3	5.11	8.47	7.71
Ti	66.5	65.5	47.4	64.6	96.9	60.4	47.0	60.3	64.6	83.3	59.9	78.1	70.3
V	7.67	5.28	5.72	6.89	8.20	6.79	6.94	5.94	6.43	18.76	5.51	4.81	6.94
Cr	264	546	658	575	277	543	264	607	299	682	763	278	446
Mn	1919	1473	1105	1272	1877	1448	1913	1086	1816	1697	1112	1525	1643
Co	193	172	158	168	191	177	190	166	181	164	167	180	184
Cu	9.38	9.12	7.34	8.12	9.91	7.57	8.50	6.69	10.2	3.92	6.48	6.35	7.65
Zn	161	113	86.8	84.0	133	98.0	125	71.9	153	93.0	73.8	91.2	90.7
Ga	55.8	61.5	53.2	48.9	43.6	44.0	39.8	72.6	48.7	54.6	67.3	35.2	37.5
Y	87.3	136	120	144	194	143	216	129	141	246	74.8	149	143
Zr	69.3	44.0	6.20	0.100	11.2	2.30	70.4	12.5	53.0	7.30		125	

样品	PCTK-7-12	PCTK-7-13	PCTK-7-14	PCTK-7-15	PCTK-7-16	PCTK-7-18	PCTK-8-2	PCTK-8-4	PCTK-8-5	PCTK-8-6	PCTK-8-7	PCTK-8-8	PCTK-8-9
SiO_2	41.03	40.03	40.38	41.22	40.22	40.23	40.33	40.08	39.47	40.46	42.01	39.51	40.38
FeO	11.28	13.05	13.03	9.51	14.02	12.58	10.26	15.46	15.75	11.55	8.57	17.57	11.99
MgO	48.29	46.46	46.13	49.73	45.01	46.04	48.29	44.69	43.93	47.74	51.23	42.94	46.49
Fo	88.41	86.38	86.32	90.32	85.13	86.70	89.35	83.75	83.25	88.05	91.42	81.34	87.36
Ni	3386	2707	3024	3640	2685	4519	3527	2835	2857	3338	4071	2466	3415
Li	0.802	0.704	0.852	1.03	3.23	1.83	2.14	1.96	0.894	0.134	0.872	0.196	1.67
Na	41.2	33.1	30.2	35.4	30.6	45.2	48.1	33.8	38.4	22.1	45.8	32.9	38.7
Al	259	308	276	232	214	493	340	267	380	356	236	248	252
P	43.6	21.2	24.2	29.4	88.7	27.1	41.0	44.2	26.2	24.5	58.7	30.8	67.9
Ca	2436	2527	2276	2436	2734	3099	2325	2619	2372	2437	1952	2622	2389
Sc	7.04	7.62	8.01	6.65	8.25	9.40	6.45	8.13	8.89	8.42	5.27	8.89	6.32
Ti	58.9	72.2	66.5	51.2	77.2	78.4	60.0	70.0	80.1	78.1	39.4	79.8	59.1
V	6.22	7.53	6.54	5.44	6.78	9.87	5.78	8.39	11.5	10.2	4.13	9.09	7.00
Cr	489	465	430	479	290	898	637	399	395	486	408	268	513
Mn	1305	1523	1554	1095	1717	2009	1266	2006	1983	1438	1116	2275	1345
Co	179	190	179	165	184	232	203	194	194	176	162	205	195
Cu	6.71	7.84	5.60	9.67	5.64	9.87	5.31	12.11	12.6	6.12	5.60	10.3	9.59
Zn	79.1	97.4	97.9	93.2	102	138	76.4	146	139.4	97.8	62.3	144	90.5
Ga	42.4	63.0	41.9	38.7	45.1	67.0	51.4	58.1	76.3	69.5	23.3	72.8	59.0
Y	168	110	132	102	177	123	129	143	182	154	133	221	115
Zr	35.0	50.4		75.7		30.6	42.7	63.8					

样品	PCTK-8-11	PCTK-8-14	PCTK-9-3	PCTK-9-4	PCTK-9-5	PCTK-9-6	PCTK-9-7	PCTK-5-1	PCTK-5-2	PCTK-5-3	PCTK-5-6	PCTK-5-8	PCTK-5-9
SiO_2	39.48	39.31	40.24	39.82	39.11	40.29	39.47	39.64	40.35	39.87	39.73	40.25	39.19
FeO	12.00	17.53	10.84	12.83	17.03	8.98	15.01	14.35	8.78	13.12	15.67	12.62	12.68
MgO	45.14	42.52	47.24	45.96	42.88	48.43	44.45	44.89	48.37	45.95	44.67	46.37	46.30
Fo	87.02	81.22	88.59	86.46	81.78	90.58	84.08	84.79	90.76	86.19	83.56	86.75	86.68
Ni	2709	2429	3699	3076	2484	3618	2727	2995	3528	3057	2591	3428	3425
Li	2.07	0.649	1.01	1.30	0.153	1.49	1.31	2.26	1.08	1.32	2.10	2.18	1.92
Na	29.2	35.4	25.6	36.8	41.5	43.6	42.5	50.8	46.6	40.6	40.9	38.3	34.0
Al	226	271	297	248	228	334	244	270	438	380	200	274	254
P	79.8	21.8	27.5	78.4	34.1	33.4	47.3	38.4	31.2	51.1	30.4	124	35.4

续表 1:

样品	PCTK-8-11	PCTK-8-14	PCTK-9-3	PCTK-9-4	PCTK-9-5	PCTK-9-6	PCTK-9-7	PCTK-5-1	PCTK-5-2	PCTK-5-3	PCTK-5-6	PCTK-5-8	PCTK-5-9
Ca	2549	2545	2098	2695	2714	2242	2622	2510	2320	2537	2955	2236	2255
Sc	7.63	9.25	6.86	7.90	8.78	6.28	7.92	7.74	7.08	7.87	8.47	6.86	6.73
Ti	63.1	103	86.5	67.0	99.9	68.5	63.5	65.3	52.7	62.9	69.3	54.2	55.7
V	6.03	10.0	5.09	7.04	9.40	6.10	7.80	8.02	7.65	7.93	7.96	5.46	5.62
Cr	319	246	469	408	255	757	280	460	788	530	281	587	533
Mn	1748	2236	1305	1588	2224	1198	1878	1821	1194	1634	1961	1516	1587
Co	200	201	162	176	201	170	203	195	175	191	198	178	177
Cu	10.0	7.96	4.07	7.42	10.5	7.36	7.77	7.84	4.58	12.7	5.91	8.28	7.72
Zn	129	144	83.8	97.8	143	86.9	114	108	62.1	115	120	101	109
Ga	57.2	41.2	57.9	51.4	50.4	74.1	62.7	53.6	64.7	57.2	41.5	44.5	51.5
Y	121	256	73.6	138	235	131	138	108	154	174	184	108	94.2
Zr	29.8	24.6	70.8	39.6	61.1	75.2	55.1	113	33.1	126	30.2	95.3	72.2

样品	PCTK-5-10	PCTK-6-1	PCTK-6-2	PCTK-6-3	PCTK-6-4	PCTK-6-5	PCTK-6-6	PCTK-6-8	PCTK-6-9	PCTK-6-10	PCTK-6-11	PCTK-6-13	PCTK-6-15
SiO_2	39.65	40.09	39.93	39.54	39.91	40.24	39.49	39.08	39.83	39.26	39.03	40.71	38.02
FeO	8.73	11.27	14.16	10.18	14.52	11.32	13.14	13.08	13.13	13.63	10.26	11.25	10.35
MgO	50.27	46.66	45.11	48.43	44.92	46.66	45.49	46.11	46.05	44.68	48.58	47.69	49.72
Fo	91.12	88.07	85.03	89.46	84.65	88.02	86.05	86.27	86.21	85.39	89.40	88.31	89.54
Ni	3937	3608	2939	3636	2737	3388	3156	3052	2863	2933	3307	3204	3681
Li	0.461	1.55	1.47	0.711	2.88	0.251	1.57	0.724	1.57	0.794	2.16	1.73	1.27
Na	47.2	32.7	45.6	24.3	68.2	35.2	34.1	39.1	40.8	32.8	45.7	45.3	40.9
Al	349	264	297	363	424	268	242	357	230	355	242	276	327
P	31.1	43.5	43.0	24.3	38.2	22.4	59.3	26.8	28.9	30.3	55.1	34.0	27.9
Ca	2275	2127	2550	2360	2541	2522	2329	2198	2407	2502	2684	2309	2210
Sc	5.53	5.52	8.06	6.95	8.20	8.18	7.88	8.10	6.59	8.73	6.72	7.31	6.62
Ti	52.6	44.0	69.1	78.2	84.5	60.4	56.7	69.5	53.5	82.8	67.3	85.7	69.3
V	5.67	5.55	8.14	7.79	9.02	6.37	10.2	8.13	5.51	8.19	5.44	5.80	6.32
Cr	772	480	454	579	332	398	312	537	435	367	481	344	611
Mn	1098	1294	1786	1256	1839	1483	1618	1589	1549	1720	1255	1424	1193
Co	159	171	185	176	189	184	180	179	187	184	179	159	172
Cu	3.34	9.95	10.3	8.24	17.7	5.65	5.78	9.10	9.40	11.0	9.15	11.7	7.75
Zn	62.6	103	126	93.3	112	74.2	103	103	113	106	88.6	86.3	79.4
Ga	57.0	60.0	53.9	55.8	78.8	64.4	55.4	59.2	38.7	58.5	49.9	65.3	67.4
Y	116	93.6	142	142	212	123	206	166	130	127	103	137	127
Zr		54.0	28.3	82.6	202	55.5		52.4	69.8	42.8	22.3	58.5	62.3

注: 主量元素单位为%; Fo 为 mol%; 微量元素中 Ga、Y 和 Zr 的单位为 ng/g, 其他微量元素单位为 μg/g。部分橄榄石微量低于检出限, 故未显示。

3 分析结果

平川苦橄岩中橄榄石主量、微量元素组成, 以及尖晶石成分见表 1 和表 2。结果显示, 平川苦橄岩中橄榄石 CaO 和 Al_2O_3 含量分别为 0.38%~0.58%和 0.037%~0.10%, 高于典型的地幔橄榄石(CaO<0.1%, Al_2O_3< 0.03%; Foley et al., 2013)。结合橄榄石中多含有尖晶石包裹体以及熔体包裹体, 表明这些橄榄石是岩浆成因。在全岩 $Mg^{\#}$与橄榄石 Fo 的图解中, 橄榄石的最高 Fo 与寄主全岩的 $Mg^{\#}$平衡, 无明显橄榄石堆晶(图 4)。橄榄石中 Ni 与 Fo 呈正相关, Ca、Mn、Sc、Co 与 Fo 呈负相关, 符合橄榄石的分离结晶趋势(图 5)。平川橄榄石 Ni 含量为 2429~4519 μg/g, Zn 含量为 62.3~161 μg/g, Co 含量为 158~232 μg/g, Sc 含量为 5.11~11.3 μg/g, Fe/Mn 值为 62.9~76.3, Mn/Zn 值高于

11.8, 100×Mn/Fe 值高于 1.31。与大理橄榄石相比, 平川橄榄石整体上具有较高 Ni、Co 含量, 较低 Ca、Mn、Sc 含量, 以及较高 Fe/Mn 和 Zn/Fe 值(图 5)。在 Ni-Mn/Zn 和 100×Mn/Fe-10000×Zn/Fe 源区判别图解中, 平川苦橄岩中橄榄石成分整体上与橄榄岩源区熔体中结晶的橄榄石成分相似, 但呈现出较高的 Zn/Fe 值和较低的 Mn/Fe 值, 其成分特征更趋向于橄榄岩源区和辉石岩源区的混合(图 2)。

平川苦橄岩中 Cr 尖晶石的 $Mg^{\#}$值具有较大变化范围($Mg^{\#}$=0.25~0.56), Cr_2O_3 含量为 41.4%~48.0%, $Cr^{\#}$为 0.43~0.72。与大理苦橄岩相比, 平川苦橄岩中尖晶石具有较低 $Mg^{\#}$值, 其 $Mg^{\#}$值更接近于高钛苦橄岩(永胜苦橄岩; Kamenetsky et al., 2012)中的尖晶石(图 6)。

4　讨　论

4.1　岩浆的氧逸度

橄榄石(Ol)−尖晶石(Sp)−斜方辉石(Opx)氧逸度计是估算地幔超基性岩氧逸度常用的方法(Ballhaus et al., 1991)。Nikolaev et al. (2016)结合不

表 2　平川苦橄岩橄榄石中尖晶石包裹体成分(%)

Table 2　Chemical compositions of the olivine-hosted Cr-spinel inclusions from the Pingchuan picrites (%)

样品	SiO_2	TiO_2	Al_2O_3	Cr_2O_3	MnO	MgO	FeO^T	NiO	V_2O_3	Total	Fe_2O_3	FeO	$Cr^{\#}$	ΔQFM
PCTK-3-4	0.084	1.26	16.47	37.98	0.30	9.39	30.77	0.21	0.21	97.86	11.77	20.18	0.607	0.23
PCTK-3-5	0.065	1.02	15.33	41.46	0.31	9.38	28.51	0.19	0.20	97.43	9.81	19.68	0.645	0.05
PCTK-3-6	0.422	3.14	24.04	26.83	0.27	10.80	30.77	0.30	0.27	97.90	10.51	21.31	0.428	0.13
PCTK-3-8	0.069	1.42	20.52	35.28	0.27	10.37	29.75	0.24	0.22	99.24	10.95	19.89	0.536	0.15
PCTK-3-9	0.069	1.69	15.64	39.13	0.29	9.67	29.39	0.20	0.25	97.38	10.58	19.87	0.627	0.27
PCTK-3-10	0.324	1.06	17.78	42.19	0.24	11.55	23.28	0.21	0.17	97.49	6.74	17.22	0.614	0.04
PCTK-3-12	0.080	1.25	15.33	35.14	0.29	8.57	34.72	0.21	0.25	97.36	15.20	21.04	0.606	0.25
PCTK-3-13	0.082	1.00	19.47	36.20	0.28	10.45	29.89	0.21	0.23	99.00	11.90	19.18	0.555	0.20
PCTK-4-1	0.056	0.49	11.80	45.98	0.33	7.84	29.14	0.14	0.16	96.86	9.22	20.84	0.723	–0.08
PCTK-4-2	0.072	0.75	15.99	47.06	0.27	11.60	19.93	0.18	0.14	96.42	4.42	15.95	0.664	0.10
PCTK-4-3	0.043	1.62	19.56	30.92	0.30	8.86	34.14	0.25	0.23	97.33	14.06	21.49	0.515	0.54
PCTK-4-5	0.048	0.95	15.18	35.69	0.35	6.91	36.82	0.19	0.21	97.84	14.96	23.36	0.612	0.40
PCTK-4-7	0.136	0.90	17.64	44.74	0.24	12.34	21.01	0.24	0.13	97.96	5.85	15.75	0.630	0.10
PCTK-4-9	0.040	1.38	19.48	31.66	0.28	8.76	34.03	0.25	0.27	97.56	13.91	21.51	0.522	0.43
PCTK-4-10	0.069	1.09	19.15	40.22	0.27	11.42	25.21	0.25	0.18	98.70	8.41	17.64	0.585	0.31
PCTK-5-1	0.080	0.94	15.87	42.19	0.30	9.32	28.69	0.20	0.20	98.74	9.41	20.22	0.641	–0.09
样品	SiO_2	TiO_2	Al_2O_3	Cr_2O_3	MnO	MgO	FeO^T	NiO	V_2O_3	Total	Fe_2O_3	FeO	$Cr^{\#}$	ΔQFM
PCTK-5-2	0.135	0.87	21.53	40.18	0.21	13.67	19.90	0.26	0.15	97.56	6.39	14.15	0.556	0.28
PCTK-5-6	0.057	1.67	20.51	34.18	0.28	10.37	31.04	0.23	0.31	99.83	11.94	20.29	0.528	0.16
PCTK-5-8	0.104	0.61	13.99	46.16	0.31	8.87	26.04	0.14	0.14	97.05	6.83	19.90	0.689	–0.16
PCTK-5-9	0.201	1.06	15.47	43.71	0.30	9.35	26.66	0.17	0.15	97.80	7.24	20.15	0.655	–0.06
PCTK-5-10	0.119	0.90	19.89	47.14	0.24	12.91	18.29	0.19	0.13	100.07	2.57	15.98	0.614	–0.52
PCTK-6-1	0.073	0.71	13.33	44.73	0.31	8.53	28.43	0.16	0.14	97.31	8.93	20.39	0.692	0.50
PCTK-6-2	0.062	0.76	17.17	38.71	0.29	8.74	30.48	0.21	0.19	97.70	10.79	20.76	0.602	0.14
PCTK-6-3	0.076	0.85	17.84	43.48	0.26	11.28	23.47	0.21	0.16	98.29	6.77	17.38	0.621	0.26
PCTK-6-4	0.117	1.06	17.32	37.86	0.30	9.05	31.25	0.20	0.24	98.54	11.46	20.93	0.595	0.03
PCTK-6-5	0.044	1.10	16.77	41.42	0.28	10.43	26.85	0.21	0.17	98.19	9.16	18.61	0.624	0.49
PCTK-6-6	0.072	0.68	18.16	39.27	0.28	9.78	28.87	0.21	0.29	98.65	10.29	19.60	0.592	0.30
PCTK-6-8	0.059	0.71	14.04	44.85	0.30	9.17	27.92	0.16	0.16	98.27	8.99	19.83	0.682	0.00
PCTK-6-9	0.062	1.30	17.29	39.18	0.32	9.34	29.75	0.21	0.19	98.67	10.11	20.65	0.603	0.36
PCTK-6-10	0.054	1.05	18.46	35.76	0.30	9.55	31.98	0.22	0.20	98.88	12.96	20.32	0.565	0.39
PCTK-6-11	0.068	1.03	17.55	42.68	0.27	11.27	24.18	0.22	0.14	98.17	7.50	17.43	0.620	0.54
PCTK-6-13	0.056	1.41	21.16	35.59	0.27	11.40	26.79	0.26	0.15	98.07	9.76	18.01	0.530	0.62
PCTK-6-15	0.080	0.90	16.27	43.00	0.26	10.40	22.89	0.24	0.15	94.81	6.11	17.39	0.639	0.25

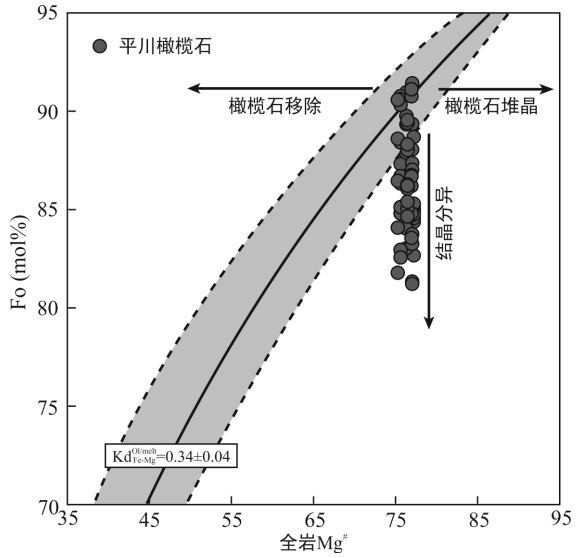

$Mg^{\#}=100\times Mg^{2+}/(Mg^{2+}+Fe^{2+})$, 假定 $Fe^{2+}/Fe^{T}=0.9$。

图 4　平川苦橄岩全岩 $Mg^{\#}$与橄榄石 Fo 图解(底图自 Putirka et al., 2007)

Fig.4　Whole-rock Mg number ($Mg^{\#}$) plotted against Fo contents of olivine crystals in the Pingchuan picrites

同氧化还原条件下的天然样品和合成样品的矿物−熔体平衡实验的最新数据, 重新评估、并改进了该公式, 并将这种方法扩展至不含斜方辉石(Opx)的矿物组合, 因此该氧逸度计也适用于基性岩浆氧逸度的估算。需要注意的是, 利用 Nikolaev et al. (2016)新公式得到的峨眉山岩浆氧逸度比利用 Ballhaus et al. (1991)公式得到的氧逸度($\log f_{O_2}$)要低约 1 个 log unit。Nikolaev et al. (2016)认为 Ballbaus et al. (1991)的公式系统高估了氧逸度环境。Nikolaev et al. (2016)实验数据的参数范围为: 温度: 1015~1500 ℃, 氧化还原条件: IW−3~NNO+1, Cr 含量: 0~16%, 压力范围 0.0001~2.7 GPa, 并且包括了含有斜方辉石和不含斜方辉石的实验矿物组合。该方法的误差约为±0.3 log units(Erdmann et al., 2019), 其公式如下:

$$\Delta\mathrm{QFM}=\frac{4720}{T}-500\frac{P}{T}-2.7\ln\frac{X_{Fe^{2+}}^{Ol}}{X_{Fe^{2+}}^{Ol}+X_{Mg}^{Ol}}-0.91\ln\frac{X_{Fe^{2+}}^{S_p}}{X_{Fe^{2+}}^{S_p}+X_{Mg}^{S_p}}-1.03\left(\ln\frac{X_{Fe^{2+}}^{S_p}}{X_{Fe^{2+}}^{S_p}+X_{Mg}^{S_p}}\right)^2+1.91\ln\frac{X_{Fe^{3+}}^{S_p}}{X_{Al}^{S_p}+X_{CR}^{S_p}+X_{Fe^{3+}}^{S_p}}+0.12\left(\ln\frac{X_{Fe^{3+}}^{S_p}}{X_{Al}^{S_p}+X_{Cr}^{S_p}+X_{Fe^{3+}}^{S_p}}\right)^2-4.4$$

其中, T 的单位为 K, P 的单位为 GPa, X^{Ol} 和 X^{Sp} 是橄榄石和尖晶石中的各离子摩尔分数。

将平川橄榄石和尖晶石包裹体的成分带入该公式。其中, 压力假定为 1.3 GPa(Tao et al., 2015), Fe^{3+}和 Fe^{2+}的摩尔分数是根据电价平衡原理计算获得, 橄榄石−尖晶石的共结温度可由 Coogan et al. (2014)提出的橄榄石−尖晶石 Al 温度计获得。Nikolaev et al. (2016)指出, 当 Fe^{3+}的含量大于 2mol%时, 估算尖晶石中 Fe^{3+}比例所产生的误差小于氧逸度计本身的误差; 当 Fe^{3+}的含量大于 10mol%时, 由估算 Fe^{3+}导致的氧逸度偏差可以忽略不计。平川尖晶石的 Fe^{3+}摩尔分数为 1.5mol%~9.5mol%, 绝大多数大于 4mol%, 由估算 Fe^{3+}引起的误差较小。通过此公式, 我们获得平川岩浆的氧逸度($\log f_{O_2}$)范围为 ΔQFM–0.5~ΔQFM+0.6, 这个氧逸度范围与洋岛玄武岩相似(ΔQFM=−0.6~+0.7; Hong et al., 2019), 低于岛弧岩浆的氧逸度(ΔQFM=+0.03~+2.5; Hong et al., 2019)。由于在岩浆分离结晶过程中, 橄榄石和尖晶石的分离结晶分别会导致岩浆氧逸度升高和降低, 因此通过高 Fo 橄榄石计算获得的氧逸度更能反映初始熔体的氧逸度。本研究中, 平川苦橄岩和大理苦橄岩最高 Fo 橄榄石具有相似的 Fo, 计算获得的平川和大理苦橄岩中 Fo>88 的橄榄石氧逸度平均值分别为 ΔQFM=+0.24 和 ΔQFM=–0.51。

此外, 橄榄石 V/Sc 值也可以指示岩浆氧逸度。V 和 Sc 在橄榄石中具有相似的分配系数, 但是在氧化环境时, V^{5+}的相对含量会比其他价态(V^{2+}, V^{3+}, V^{4+})高(Li and Lee, 2004; Lee et al., 2005)。V^{5+}的增加会导致 V 在橄榄石−熔体间的分配系数降低, 导致 V 在氧化条件下更不相容(Canil, 1997), 所以高氧逸度环境下结晶的橄榄石通常具有较低的 V/Sc 值(Foley et al., 2013)。平川橄榄石 V/Sc 值整体上与橄榄石−尖晶石氧逸度计得出的氧逸度呈负相关关系(图 7), 表明平川苦橄岩母岩浆比大理苦橄岩母岩浆具有更高的氧逸度。影响岩浆氧逸度的因素较多, 部分熔融程度、部分熔融方式、压力(深度)以及交代作用等均可造成岩浆氧逸度的差异(Wood et al., 1990; Kress and Carmichael, 1991; Dixon et al., 1997; Brounce et al., 2014; Gaetani, 2016; 柏中杰等, 2019)。峨眉山大火成岩省中, 高钛岩浆熔融程度低于低钛岩浆(Shellnut and Jahn, 2011; Ren et al., 2017; Zhang et al., 2019a; Xu et al., 2020)。平川苦橄岩较大理苦橄岩具有更高 Ti/Y 值, 表明前者的熔融程度相对较低。前人研究发现低熔融程度的岩浆通常具有

更高的氧逸度(Dixon et al., 1997; Mungall et al., 2006)。由于 Fe^{3+}在部分熔融过程中是不相容的, 低程度部分熔融的熔体倾向于具有更高的 Fe^{3+}/Fe^{T} 值(Herzberg and Asimow, 2008; Gaetani, 2016), 因此它们也应具有较高的氧逸度。然而最近对尖晶石橄榄岩部分熔体的研究表明, 源区残留的尖晶石会缓冲

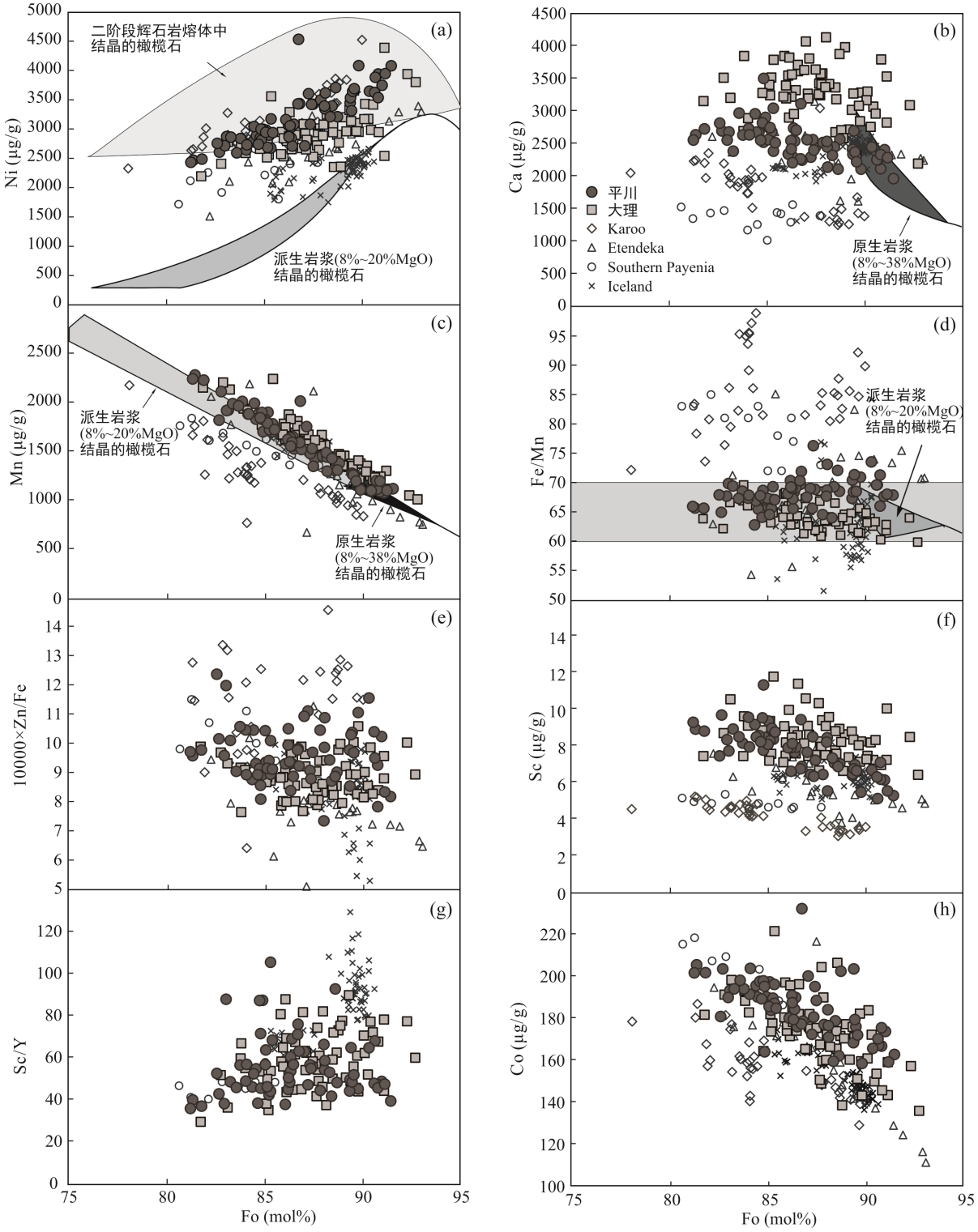

图 5　平川和大理苦橄岩中橄榄石 Ni、Ca、Mn、Fe/Mn、10000×Zn/Fe、Sc、Sc/Y 和 Co 与橄榄石 Fo 的相关关系图(a~d 中底图来自 Herzberg, 2011; 数据来源同图 2)

Fig.5　Plots of Ni, Ca, Mn, Fe/Mn, 10000×Zn/Fe, Sc, Sc/Y, and Co against Fo for the olivines from the Pingchuan and Dali picrites

岩浆中 Fe^{3+}/Fe^{T}值, 因此对于尖晶石橄榄岩源区, 部分熔融程度差异对岩浆氧逸度的改变很有限(Davis and Cottrell, 2018; Sorbadere et al., 2018)。但是峨眉山大火成岩省的研究表明部分熔融发生在石榴石相(Zhang et al., 2019a), 因此本研究初步认为部分熔融程度的差异可能是导致平川苦橄岩母岩浆和大理苦橄岩母岩浆氧逸度差异的主要因素之一。

4.2 平川苦橄岩的源区岩性

除了传统观点认为的辉石岩源区熔体中结晶的橄榄石比橄榄岩源区熔体中结晶的橄榄石具有高 Ni

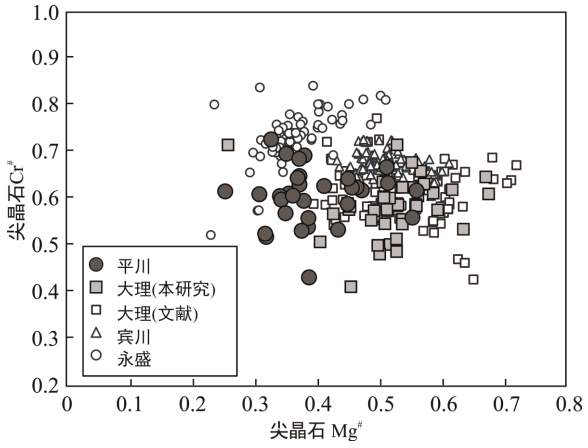

宾川苦橄岩(Ti/Y=297)和永胜苦橄岩(Ti/Y_{mean}=790)中的尖晶石数据来自 Kamenetsky et al. (2012)。大理尖晶石文献数据来自 Kamenetsky et al. (2012) 和 Liu et al. (2017)。($Cr^{\#}$=Cr/(Cr+Al); $Mg^{\#}$=Mg/(Mg+Fe^{2+}), molar)。

图 6 橄榄石中的尖晶石包裹体 $Cr^{\#}$-$Mg^{\#}$关系图

Fig.6 Plots of $Cr^{\#}$ *vs.* $Mg^{\#}$ of the olivine hosted spinel inclusions

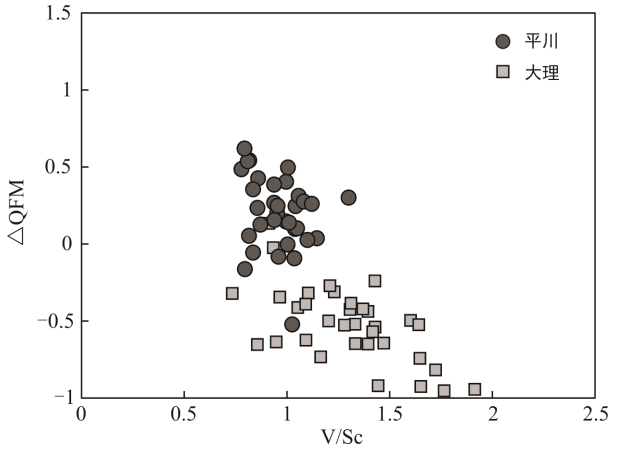

橄榄石−尖晶石共结时熔体的氧逸度(ΔQFM)是利用 Nikolaev et al. (2016)的橄榄石−尖晶石氧逸度公式计算的。氧逸度(ΔQFM)和橄榄石 V/Sc 整体具有负相关性。

图 7 氧逸度(ΔQFM)-橄榄石 V/Sc 值图

Fig.7 Plots of oxygen fugacity (log fo_2 QFM) *vs.* V/Sc of the olivines

含量、Fe/Mn 值, 低 Ca、Mn 含量特征外(Sobolev et al., 2007; Herzberg, 2011), 也可以通过橄榄石微量元素特征对源区组分进行识别。比如, 辉石岩相对于橄榄岩具有低 Zn 和 Co 的全岩−熔体分配系数(Le Roux et al., 2011; Davis et al., 2013), 因此, 与橄榄岩熔体相比, 辉石岩熔体会具有更高的 Zn 和 Co 含量。而且在组成地幔的主要矿物中, Sc 更相容于单斜辉石, 因此辉石岩熔体相比橄榄岩熔体也会呈现出较低 Sc 含量和 Sc/Y 值。此外, 橄榄石中 Zn/Fe 值也可以用来识别源区特征(Le Roux et al., 2011; Foley et al., 2013; Lee, 2014)。Zn/Fe 值在橄榄石、斜方辉石与熔体间的分配系数为 1, Zn/Fe 值在橄榄岩熔融时基本不会发生分馏; 而单斜辉石和石榴子石相比橄榄石、斜方辉石和熔体之间具有低的 Zn/Fe 分配系数, 因此富含石榴子辉石岩的源区熔融, 产生的熔体相比其源区会具有高 Zn/Fe 值(Lee, 2014)。而且氧逸度也会影响岩浆中 Zn/Fe 值, 高氧逸度环境下, 熔体具有更高 Fe^{3+}/Fe^{2+}值。Fe^{3+}比 Fe^{2+}更不相容, 因此熔体会具有较高的 Fe 含量, 导致熔体中 Zn/Fe 值较低(Le Roux et al., 2010)。由于平川岩浆的氧逸度高于大理岩浆(图 7), 若主要是氧逸度造成平川苦橄岩和大理苦橄岩中橄榄石 Zn/Fe 值差异, 则平川橄榄石应比大理橄榄石具有更低 Zn/Fe 值, 而本次研究结果显示平川苦橄岩中橄榄石 Zn/Fe 值高于大理苦橄岩中的橄榄石(图 5), 因此平川苦橄岩和大理苦橄岩中橄榄石 Zn/Fe 值差异不是氧逸度引起的。综合平川橄榄石比大理橄榄石显示出的更高 Ni、Co 含量和 Zn/Fe、Fe/Mn 值, 低 Ca、Mn、Sc 含量和 Mn/Zn 值等特征(图 2、5), 指示了平川苦橄岩源区中可能存在辉石岩组分。

近年来, 不断有学者开始关注峨眉山大火成岩省中的源区组分, 尤其是再循环物质的存在(Zhong et al., 2011; Ren et al., 2017; Yu et al., 2017; Yang and Liu. 2019; Zhang et al., 2019a; Zhang et al., 2021), 一些研究者认为再循环组分对成矿具有关键作用(Hou et al., 2013; Bai et al., 2014; Yu et al., 2014)。地幔、地核以及硅酸盐地球(BSE)的 Ni/Co 值在 20 左右, 橄榄石以及尖晶石的分离结晶会导致 Ni/Co 值降低, Ni/Co 值高于 BSE 可以指示地幔源区中有再循环洋壳物质的存在(Sobolev et al., 2007; Foley et al., 2013; Howarth and Harris, 2017), 或者含有高 Ni/Co 值矿物(如金云母)的再循环陆壳物质存在。具有高 Fo 的平川和大理橄榄石普遍具有较高 Ni/Co 值, 暗示在峨眉山大火成岩省源区中可能存在少量俯冲物质的

再循环(图 8)。Foley et al. (2013)进一步提出橄榄石中 Li 含量也可以用来区分源区中的再循环洋壳与陆壳。相比于岩石圈地幔以及洋壳, Li 元素更富集于陆壳以及陆源沉积物中(Rudnick and Gao, 2003), 因此陆壳物质再循环会携带高 Li 信息进入地幔(Prelevic et al., 2013)。虽然 Li 作为不相容元素($Kd_{\mathrm{Li}}^{\mathrm{ol-liq}}=0.35$; Nikogosyan and Sobolev, 1997), 熔体中 Li 含量会受部分熔融程度的影响, 但受陆壳再循环物质影响的地幔源区产生的熔体会具有明显高 Li 含量, 比如罗清晨等(2020)报道的我国东北地区(加格达奇)早白垩世苦橄岩中的橄榄石(图 9)。而平川和大理苦橄岩中的橄榄石 Li 含量较低, 说明峨眉山大火成岩省的地幔源区中没有明显的再循环陆壳物质加入。而再循环洋壳(以及少量沉积物)进入地幔, 可能通过固−固混合的方式与橄榄岩地幔混合, 也可能是俯冲再循环洋壳产生的熔体交代橄榄岩形成二阶段辉石岩, 二阶段辉石岩与残余橄榄岩熔融产生具有辉石岩特征的熔体(Sobolev et al., 2007; Herzberg, 2011; Delavault et al., 2015; Frey et al., 2016; Huang and Zheng, 2017; Hole and Natland, 2019)。因此, 在峨眉山大火成岩省, 再循环洋壳加入橄榄岩地幔极有可能形成含有辉石岩组分的源区。

在橄榄岩−辉石岩源区的判别图中, 平川苦橄岩中橄榄石样品点普遍落在橄榄岩源区范围内, 并不具有明显辉石岩源区熔体中结晶的橄榄石的特征(图 2)。无橄榄石辉石岩部分熔融产生的熔体成分受源区中辉石矿物组分的控制明显, 其结晶的橄榄石会具有明显的高 Ni、Co 含量, 高 Fe/Mn、Zn/Fe 值, 低 Mn、Ca 含量, 以及低 Sc/Y、Mn/Zn 值特征。但峨眉山大火成岩省的地幔源区是含有橄榄石的而不是无橄榄石辉石岩。无橄榄石辉石岩产生的熔体 MgO 含量较低(MgO<15%; Yang et al., 2016), 而峨眉山大火成岩省初始熔体的 MgO 可达 23.2%(Zhang et al., 2006; Hanski et al., 2010; Ren et al., 2017)。橄榄岩和辉石岩成分是过渡变化的, 主要区别在于源区矿物中橄榄石的比例。根据 Le Maître et al. (2002)的定义, 由橄榄石、辉石、石榴子石为主要成分, 其中橄榄石含量小于 40%的地幔岩为辉石岩。而进入地幔的再循环洋壳会影响地幔源区中的矿物组成, 即随着进入地幔橄榄岩的再循环洋壳比例增加, 橄榄岩与再循环物质产生的熔体反应, 逐渐消耗橄榄石, 转变为辉石岩。再循环洋壳与亏损地幔混合的比例不同, 形成地幔源区中的橄榄石所占的比例也不同。根据 Yang et al. (2016)的模型, 若 10%再循环洋壳加入到亏损地幔中, 形成的源区含有约 60%的橄榄石; 若 30%再循环洋壳加入到亏损地幔中时, 源区中的橄榄石含量降低到约 40%, 根据定义这种地幔源区可以称之为辉石岩, 如 KG2 辉石岩(实验辉石岩, 成分相当于 67%富集的尖晶石二辉橄榄 KLB-1 与 33%平均 MORB 的混合物; Kogiso et al., 1998); 若 70%再循环洋壳加入亏损地幔时, 则形成无橄榄石辉石岩, 类似于 MIX1G(近似于典型地幔辉石岩, 为两块来自 Balmuccia 地块天然辉石岩的混合物; Hirschmann et al., 2003)。

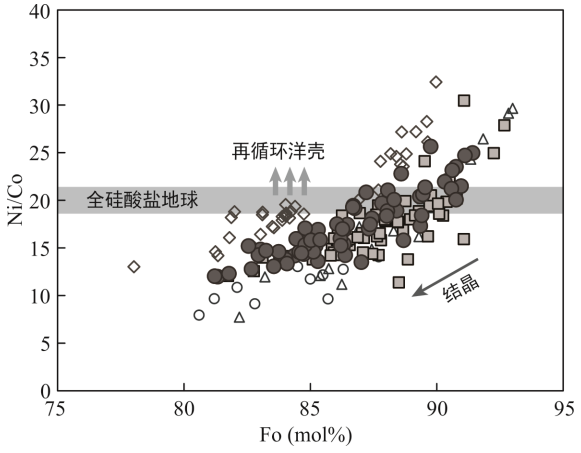

Ni/Co>20 指示源区中存在再循环壳源物质(Sobolev et al., 2007; Foley et al., 2013)。Howarth and Harris (2017)认为 Ni/Co>20 也可以指示地幔源区中辉石岩组分的存在。

图 8　平川和大理苦橄岩中橄榄石 Ni/Co 与 Fo 相关关系图

Fig.8　Plots of Ni/Co *vs.* Fo of the olivines from the Pingchuan and Dali picrites

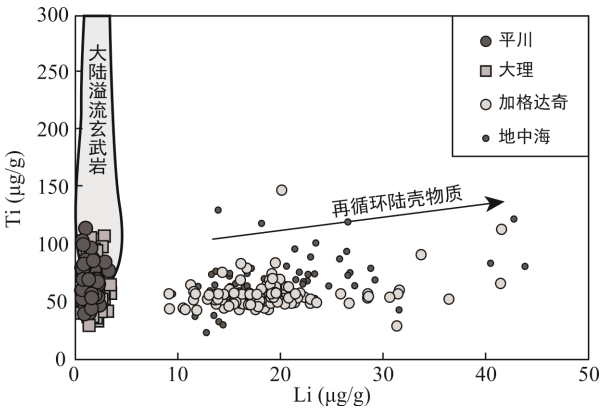

地中海钾镁煌斑岩中橄榄石成分来自 Prelevic et al. (2013); 典型大陆溢流玄武岩橄榄石成分范围来自 Foley et al. (2013); 加格达奇早白垩世苦橄岩中的橄榄石来自含有再循环陆壳的源区(罗清晨等, 2020)。

图 9　平川和大理苦橄岩中橄榄石 Ti 与 Li 相关关系图

Fig.9　Plots of Ti *vs.* Li of the olivines from the Pingchuang and Dali picrites

Yang and Liu (2019)、Zhang et al. (2019a, 2021)通过丽江苦橄岩 Mg 同位素, 丽江、大理苦橄岩熔体包裹体微量元素及同位素研究, 估算出峨眉山大火成岩省源区组分中含有约 15%(0~20%)的再循环洋壳。根据 Yang et al. (2016)的模型, 15%的再循环洋壳与亏损地幔混合会形成含橄榄石的混合源区(类似 KG2 辉石岩, 但具有更高的橄榄石/辉石比例), 这种地幔源区产生的熔体中结晶的橄榄石成分特征可能与平川橄榄石类似, 仍近似于橄榄岩熔体中结晶的橄榄石成分, 但同时橄榄石成分也显示出源区中存在辉石岩组分的控制, 具有较大的变化范围。这或许也是平川和大理橄榄石样品均主要落在橄榄岩区域, 但成分上又有明显差异的原因。在 Howarth and Harris (2017)的判别图中, Iceland 玄武岩橄榄石成分也出现类似情况(图 2、5), Iceland 地幔源区被认为含有约 10%富集的辉石岩组分(Shorttle et al., 2014; Neave et al., 2018; Hole and Natland, 2019), 但 Iceland 橄榄石成分也基本落在橄榄岩区域。而且前人研究也发现, 由于辉石岩源区成分以及矿物组成极不均一, 其产生的岩浆也是多样的, 可能产生成分类似于橄榄岩源区的岩浆, 尤其贫 Si 含橄榄石辉石岩熔体成分与橄榄岩并没有多大区别(Lambart et al., 2016; Lambart, 2017; Hole, 2018)。因此, 橄榄石成分在判别图解中与典型橄榄石区域一致的, 其源区不一定是不含有辉石岩的。

5 结 论

(1) 平川苦橄岩岩浆氧逸度高于大理苦橄岩, 指示了峨眉山大火成岩省中高钛岩浆具有更高的氧逸度。

(2) 平川苦橄岩中橄榄石主量元素以及微量元素成分特征支持其源区可能存在辉石岩组分的控制, 区别于纯的橄榄岩源区。平川橄榄石成分符合少量再循环洋壳进入橄榄岩源区形成的混合地幔源区熔体中结晶的橄榄石成分特征。由于峨眉山大火成岩省地幔源区中再循环洋壳的平均含量较低, 导致源区矿物组成中整体上具有较低的单斜辉石比例, 因此橄榄石成分在橄榄岩-辉石岩判别图中整体投在了橄榄岩范围。

致谢: 电子探针测试得到中国科学院广州地球化学研究所陈林丽工程师、贺鹏丽工程师和杨帆博士后的大力帮助, 两位匿名审稿人对本文提出了宝贵意见, 在此一并表示感谢。

参考文献(References):

柏中杰, 钟宏, 朱维光. 2019. 幔源岩浆氧化还原状态及对岩浆矿床成矿的制约. 岩石学报, 35(1): 204–214.

罗清晨, 任钟元, 张乐, 徐晓波. 2020 大兴安岭中生代玄武岩成因及深部动力学机制. 地球化学, 49(2): 168–192.

宋谢炎, 陈列锰, 于宋月, 陶琰, 佘宇伟, 栾燕, 张晓琪, 何海龙. 2018. 峨眉大火成岩省钒钛磁铁矿矿床地质特征及成因. 矿物岩石地球化学通报, 37(6): 1003–1018.

王焰, 王坤, 邢长明, 魏博, 董欢, 曹永华. 2017. 二叠纪峨眉山地幔柱岩浆成矿作用的多样性. 矿物岩石地球化学通报, 36(3): 404–417.

吴亚东. 2018. 峨眉山大火成岩省源区性质和岩浆演化过程: 来自于苦橄岩熔体包裹体和矿物的制约. 广州: 中国科学院大学博士学位论文: 65–68.

张乐. 2019. 峨眉山大火成岩省中高钛和低钛镁铁质岩浆成因–熔体包裹体和微量元素模拟的研究. 广州: 中国科学院大学博士学位论文: 45–78.

Ali J R, Lo C H, Thompson G M, Song X Y. 2004. Emeishan Basalt Ar-Ar overprint ages define several tectonic events that affected the western Yangtze platform in the Mesozoic and Cenozoic. *Journal of Asian Earth Sciences*, 23(2): 163–178.

Anh T V, Pang K N, Chung S L, Lin H M, Hoa T T, Anh T T, Yang H J. 2011. The Song Da magmatic suite revisited: A petrologic, geochemical and Sr-Nd isotopic study on picrites, flood basalts and silicic volcanic rocks. *Journal of Asian Earth Sciences*, 42(6): 1341–1355.

Bai Z J, Zhong H, Hu R Z, Zhu W G, Hu W J. 2019. Composition of the chilled marginal rocks of the Panzhihua layered intrusion, Emeishan Large Igneous Province, SW China: Implications for parental magma compositions, sulfide saturation history, and Fe-Ti oxide mineralization. *Journal of Petrology*, 60(3): 619–648.

Bai Z J, Zhong H, Li C S, Zhu W G, He D F, Qi L. 2014. Contrasting parental magma compositions for the Hongge and Panzhihua magmatic Fe-Ti-V oxide deposits, Emeishan Large Igneous Province, SW China. *Economic Geology*, 109(6): 1763–1785.

Ballhaus C, Berry R F, Green D H. 1991. High pressure experimental calibration of the olivine-orthopyroxene-spinel oxygen geobarometer: Implications for the oxidation state of the upper mantle. *Contributions to Mineralogy and Petrology*, 107(1): 27–40.

Batanova V G, Thompson J M, Danyushevsky L V, Portnyagin

M V, Garbe-Schönberg D, Hauri E, Kimura J I, Chang Q, Senda R, Goemann K, Chauvel C, Campillo S, Ionov D A, Sobolev A V. 2019. New olivine reference material for *in situ* microanalysis. *Geostandards and Geoanalytical Research*, 43(3): 453–473.

Brounce M N, Kelley K A, Cottrell E. 2014. Variations in $Fe^{3+}/\sum Fe$ of Mariana arc basalts and mantle wedge fo_2. *Journal of Petrology*, 55(12): 2513–2536.

Bryan S E, Ernst R E. 2008. Revised definition of large igneous provinces (LIPs). *Earth-Science Reviews*, 86(1–4): 175–202.

Canil D. 1997. Vanadium partitioning and the oxidation state of Archaean komatiite magmas. *Nature*, 389(6653): 842–845.

Cao Y H, Wang C Y, Huang F, Zhang Z F. 2019. Iron isotope systematics of the Panzhihua mafic layered intrusion associated with giant Fe-Ti oxide deposit in the Emeishan Large Igneous Province, SW China. *Journal of Geophysical Research*: *Solid Earth*, 124(1), 358–375.

Chung S L, Jahn B M. 1995. Plume-lithosphere interaction in generation of the Emeishan flood basalts at the Permian-Triassic boundary. *Geology*, 23(10): 889–892.

Chung S L, Jahn B M, Genyao W, Lo C H, Bolin C. 1998. The Emeishan flood basalt in SW China: A mantle plume initiation model and its connection with continental breakup and mass extinction at the Permian-Triassic boundary // Flower M F J, Chung S L, Lo C H, Lee T Y. Mantle Dynamics and Plate Interactions in East Asia. Washington, D C: American Geophysical Union: 47–58.

Coffin M F, Eldholm O. 1992. Volcanism and continental break-up: A global compilation of large igneous provinces. *Geological Society*, *London*, *Special Publications*, 68(1): 17–30.

Coogan L, Saunders A, Wilson R. 2014. Aluminum-in-olivine thermometry of primitive basalts: Evidence of an anomalously hot mantle source for large igneous provinces. *Chemical Geology*, 368: 1–10.

Davis F A, Cottrell E. 2018. Experimental investigation of basalt and peridotite oxybarometers: Implications for spinel thermodynamic models and Fe^{3+} compatibility during generation of upper mantle melts. *American Mineralogist*, 103(7): 1056–1067.

Davis F A, Humayun M, Hirschmann M M, Cooper R S. 2013. Experimentally determined mineral/melt partitioning of first-row transition elements (FRTE) during partial melting of peridotite at 3 GPa. *Geochimica et Cosmochimica Acta*, 104: 232–260.

Delavault H, Chauvel C, Sobolev A, Batanova V. 2015. Combined petrological, geochemical and isotopic modeling of a plume source: Example of Gambier Island, Pitcairn chain. *Earth and Planetary Science Letters*, 426: 23–35.

Dixon J E, Clague D A, Wallace P, Poreda R. 1997. Volatiles in alkalic basalts form the North arch volcanic field, Hawaii: Extensive degassing of deep submarine- erupted alkalic series lavas. *Journal of Petrology*, 38(7): 911–939.

Erdmann S, Chen L H, Liu J Q, Xue X Q, Wang X J. 2019. Hot, volatile-poor, and oxidized magmatism above the stagnant Pacific plate in Eastern China in the Cenozoic. *Geochemistry*, *Geophysics*, *Geosystems*, 20(11): 4849–4868.

Fan W M, Zhang C H, Wang Y J, Guo F, Peng T P. 2008. Geochronology and geochemistry of Permian basalts in western Guangxi Province, Southwest China: Evidence for plume-lithosphere interaction. *Lithos*, 102(1–2).

Foley S F, Prelevic D, Rehfeldt T, Jacob D E. 2013. Minor and trace elements in olivines as probes into early igneous and mantle melting processes. *Earth and Planetary Science Letters*, 363: 181–191.

Frey F A, Huang S C, Xu G P, Jochum K P. 2016. The geochemical components that distinguish Loa-and Kea-trend Hawaiian shield lavas. *Geochimica et Cosmochimica Acta*, 185: 160–181.

Gaetani G A. 2016. The behavior of $Fe^{3+}/\sum Fe$ during partial melting of spinel lherzolite. *Geochimica et Cosmochimica Acta*, 185: 64–77.

Gavrilenko M, Herzberg C, Vidito C, Carr M J, Tenner T, Ozerov A. 2016. A calcium-in-olivine geohygrometer and its application to subduction zone magmatism. *Journal of Petrology*, 57(9): 1811–1832.

Hanski E, Kamenetsky V S, Luo Z Y, Xu Y G, Kuzmin D V. 2010. Primitive magmas in the Emeishan large igneous province, southwestern China and northern Vietnam. *Lithos*, 119(1–2): 75–90.

Hanski E, Walker R J, Huhma H, Polyakov G V, Balykin P A, Hoa T T, Phuong N T. 2004. Origin of the Permian-Triassic komatiites, northwestern Vietnam. *Contributions to Mineralogy and Petrology*, 147(4): 453–469.

Harris C, le Roux P, Cochrane R, Martin L, Duncan A R, Marsh J S, le Roex A P, Class C. 2015. The oxygen isotope composition of Karoo and Etendeka picrites: High $\delta^{18}O$ mantle or crustal contamination? *Contributions*

to Mineralogy and Petrology, 170(1): 1–24.

He B, Xu Y G, Chung S L, Xiao L, Wang Y M. 2003. Sedimentary evidence for a rapid, kilometer-scale crustal doming prior to the eruption of the Emeishan flood basalts. *Earth and Planetary Science Letters*, 213(3–4): 391–405.

Heinonen J S, Fusswinkel T. 2017. High Ni and low Mn/Fe in olivine phenocrysts of the Karoo meimechites do not reflect pyroxenitic mantle sources. *Chemical Geology*, 467: 134–142.

Herzberg C. 2011. Identification of source lithology in the Hawaiian and Canary islands: Implications for origins. *Journal of Petrology*, 52: 113–146.

Herzberg C, Asimow P D. 2008. Petrology of some oceanic island basalts: PRIMELT2. XLS software for primary magma calculation. *Geochemistry*, *Geophysics*, *Geosystems*, 9(9): Q09001.

Hirschmann M M, Kogiso T, Baker M B, Stolper E M. 2003. Alkalic magmas generated by partial melting of garnet pyroxenite. *Geology*, 31(6): 481–484.

Hole M J. 2018. Mineralogical and geochemical evidence for polybaric fractional crystallization of continental flood basalts and implications for identification of peridotite and pyroxenite source lithologies. *Earth-Science Reviews*, 176: 51–67.

Hole M J, Natland J H. 2019. Magmatism in the North Atlantic Igneous Province: Mantle temperatures, rifting and geodynamics. *Earth-Science Reviews*, 206, 102794.

Hong L B, Xu Y G, Zhang L, Liu Z, Xia X P, Kuang Y S. 2019. Oxidized Late Mesozoic subcontinental lithospheric mantle beneath the eastern North China Craton: A clue to understanding cratonic destruction. *Gondwana Research*, 81: 230–239.

Hou T, Zhang Z C, Encarnacion J, Santosh M, Sun Y L. 2013. The role of recycled oceanic crust in magmatism and metallogeny: Os-Sr-Nd isotopes, U-Pb geochronology and geochemistry of picritic dykes in the Panzhihua giant Fe-Ti oxide deposit, central Emeishan large igneous province, SW China. *Contributions to Mineralogy and Petrology*, 165(4): 805–822.

Hou T, Zhang Z C, Kusky T, Du Y S, Liu J L, Zhao Z D. 2011. A reappraisal of the high-Ti and low-Ti classification of basalts and petrogenetic linkage between basalts and mafic-ultramafic intrusions in the Emeishan Large Igneous Province, SW China. *Ore Geology Reviews*, 41(1): 133–143.

Hou T, Zhang Z C, Pirajno F. 2012. A new metallogenic model of the Panzhihua giant V-Ti-iron oxide deposit (Emeishan Large Igneous Province) based on high-Mg olivine-bearing wehrlite and new field evidence. *International Geology Review*, 54: 1721–1745.

Howarth G H, Harris C. 2017. Discriminating between pyroxenite and peridotite sources for continental flood basalts (CFB) in southern Africa using olivine chemistry. *Earth and Planetary Science Letters*, 475: 143–151.

Huang H, Du Y S, Yang J H, Zhou L, Hu L S, Huang H W, Huang Z Q. 2014. Origin of Permian basalts and clastic rocks in Napo, Southwest China: Implications for the erosion and eruption of the Emeishan large igneous province. *Lithos*, 208: 324–338.

Huang S C, Zheng Y F. 2017. Mantle geochemistry: Insights from ocean island basalts. *Science China Earth Sciences*, 60(11): 1976–2000.

Humayun M, Qin L P, Norman M D. 2004. Geochemical evidence for excess iron in the mantle beneath Hawaii. *Science*, 306(5693): 91–94.

Kamenetsky V S, Chung S L, Kamenetsky M B, Kuzmin D V. 2012. Picrites from the Emeishan Large Igneous Province, SW China: A compositional continuum in primitive magmas and their respective mantle sources. *Journal of Petrology*, 53(10): 2095–2113.

Kamenetsky V S, Maas R, Kamenetsky M B, Yaxley G M, Ehrig K, Zellmer G F, Bindeman I N, Sobolev A V, Kuzmin D V, Ivanov A V, Woodhead J, Schilling J G. 2017. Multiple mantle sources of continental magmatism: Insights from “high-Ti” picrites of Karoo and other large igneous provinces. *Chemical Geology*, 455: 22–31.

Kogiso T, Hirose K, Takahashi E. 1998. Melting experiments on homogeneous mixtures of peridotite and basalt: Application to the genesis of ocean island basalts. *Earth and Planetary Science Letters*, 162(1–4): 45–61.

Kress V C, Carmichael I S E. 1991. The compressibility of silicate liquids containing Fe_2O_3 and the effect of composition, temperature, oxygen fugacity and pressure on their redox states. *Contributions to Mineralogy and Petrology*, 108(1–2): 82–92.

Lai S C, Qin J F, Li Y F, Li S Z, Santosh M. 2012. Permian high Ti/Y basalts from the eastern part of the Emeishan Large Igneous Province, southwestern China: Petrogenesis and tectonic implications. *Journal of Asian Earth Sciences*, 47: 216–230.

Lambart S, Baker M B, Stolper E M. 2016. The role of

pyroxenite in basalt genesis: Melt-PX, a melting parameterization for mantle pyroxenites between 0.9 and 5 GPa. *Journal of Geophysical Research*: *Solid Earth*, 121(8): 5708–5735.

Lambart S. 2017. No direct contribution of recycled crust in Icelandic basalts. *Geochemical Perspectives Letters*, 4: 7–12.

Le Maître R W. Streckeisen A, Zanettin B, Le Bas M J, Bonin B, Bateman P, Bellieni G, Dudek A, Efremova S, Keller J, Lameyre J, Sabine P A, Schmid R, Sorensen H, Woolley A R. 2002. Igneous Rocks: A Classification and Glossary of Terms: Recommendations of the International Union of Geological Sciences Subcommission on the Systematics of Igneous Rocks. Cambridge: Cambridge University Press: 236.

Le Roux V, Dasgupta R, Lee C T A. 2011. Mineralogical heterogeneities in the Earth's mantle: Constraints from Mn, Co, Ni and Zn partitioning during partial melting. *Earth and Planetary Science Letters*, 307(3–4): 395–408.

Le Roux V, Lee C T A, Turner S J. 2010. Zn/Fe systematics in mafic and ultramafic systems: Implications for detecting major element heterogeneities in the Earth's mantle. *Geochimica et Cosmochimica Acta*, 74(9): 2779–2796.

Lee C T A. 2014. Physics and chemistry of deep continental crust recycling // Holland H D, Turekian K K. Treatise on Geochemistry. Amsterdam: Elsevier: 423–456.

Lee C T A, Leeman W P, Canil D, Li Z X A. 2005. Similar V/Sc systematics in MORB and arc basalts: Implications for the oxygen fugacities of their mantle source regions. *Journal of Petrology*, 46: 2313–2336.

Li J, Xu J F, Suzuki K, He B, Xu Y G, Ren Z Y. 2010. Os, Nd and Sr isotope and trace element geochemistry of the Muli picrites: Insights into the mantle source of the Emeishan Large Igneous Province. *Lithos*, 119(1–2): 108–122.

Li Y J, He H Y, Ivanov A V, Demonterova E I, Pan Y X, Deng C L, Zheng D W, Zhu R X. 2017. $^{40}Ar/^{39}Ar$ age of the onset of high-Ti phase of the Emeishan volcanism strengthens the link with the end-Guadalupian mass extinction. *International Geology Review*, 60(15): 1906–1917.

Li Z X A, Lee C T A. 2004. The constancy of upper mantle fo_2 through time inferred from V/Sc ratios in basalts. *Earth and Planetary Science Letters*, 228: 483–493.

Liu J, Xia Q K, Kuritani T, Hanski E, Yu H R. 2017. Mantle hydration and the role of water in the generation of large igneous provinces. *Nature Communications*, 8(1): 1824.

Liu X J, Liang Q D, Li L Z, Castillo P R, Shi Y, Xu J F, Huang X L, Liao S, Huang W L, Wu W N. 2016. Origin of Permian extremely high Ti/Y mafic lavas and dykes from western Guangxi, SW China: Implications for the Emeishan mantle plume magmatism. *Journal of Asian Earth Sciences*, 141: 97–111.

Mallmann G, O'Neill H S C. 2013. Calibration of an empirical thermometer and oxybarometer based on the partitioning of Sc, Y and V between olivine and silicate melt. *Journal of Petrology*, 54(5): 933–949.

Matzen A K, Wood B J, Baker M B, Stolper E M. 2017. The roles of pyroxenite and peridotite in the mantle sources of oceanic basalts. *Nature Geoscience*, 10(7): 530–535.

Mungall J E, Hanley J J, Arndt N T, Debecdelievre A. 2006. Evidence from meimechites and other low-degree mantle melts for redox controls on mantle-crust fractionation of platinum-group elements. *Proceedings of the National Academy of Sciences*, 103(34): 12695–12700.

Neave D A, Shorttle O, Oeser M, Weyer S, Kobayashi K. 2018. Mantle-derived trace element variability in olivines and their melt inclusions. *Earth and Planetary Science Letters*, 483: 90–104.

Nikogosyan I K, Sobolev A V. 1997. Ion-Microprobe analysis of melt inclusions in olivine: Experience in estimating the olivine-melt partition coefficients of trace elements. *Geochemistry International*, 35(2): 155–157.

Nikolaev G S, Ariskin A A, Barmina G S, Nazarov M A, Almeev R R. 2016. Test of the Ballhaus-Berry-Green Ol-Opx-Sp oxybarometer and calibration of a new equation for estimating the redox state of melts saturated with olivine and spinel. *Geochemistry International*, 54(4): 301–320.

Prelevic D, Jacob D E, Foley S F. 2013. Recycled continental crust is an essential ingredient of Mediterranean orogenic mantle lithosphere. *Earth and Planetary Science Letters*, 362: 187–197.

Putirka K D, Perfit M, Ryerson F J, Jackson M G. 2007. Ambient and excess mantle temperatures, olivine thermometry, and active *vs.* passive upwelling. *Chemical Geology*, 241(3–4): 177–206.

Ren Z Y, Ingle S, Takahashi E, Hirano N, Hirata T. 2005. The chemical structure of the Hawaiian mantle plume. *Nature*, 436: 837–840.

Ren Z Y, Wu Y D, Zhang L, Nichols A R, Hong L B, Zhang

Y H, Zhang Y, Liu J Q, Xu Y G. 2017. Primary magmas and mantle sources of Emeishan basalts constrained from major element, trace element and Pb isotope compositions of olivine-hosted melt inclusions. *Geochimica et Cosmochimica Acta*, 208: 63–85.

Rudnick R L, Gao S. 2003. Composition of the continental crust // Holland H D, Turekian K K. Treatise on Geochemistry. Amsterdam: Elsevier: 659.

Shellnutt J G, Jahn B M. 2011. Origin of Late Permian Emeishan basaltic rocks from the Panxi region (SW China): Implications for the Ti-classification and spatial-compositional distribution of the Emeishan flood basalts. *Journal of Volcanology and Geothermal Research*, 199(1–2): 85–95.

Shellnutt J G, Pham T T, Denyszyn S W, Yeh M W, Tran T A. 2020. Magmatic duration of the Emeishan large igneous province: Insight from northern Vietnam. *Geology*, 48(5): 457–461.

Shorttle O, Maclennan J, Lambart S. 2014. Quantifying lithological variability in the mantle. *Earth and Planetary Science Letters*, 395: 24–40.

Søager N, Portnyagin M, Hoernle K, Holm P M, Hauff F, Garbe-Schönberg D. 2015. Olivine major and trace element compositions in southern Payenia basalts, Argentina: Evidence for pyroxenite-peridotite melt mixing in a back-arc setting. *Journal of Petrology*, 56(8): 1495–1518.

Sobolev A V, Hofmann A W, Kuzmin D V, Yaxley G M, Arndt N T, Chung S L, Danyushevsky L V, Elliott T, Frey F A, Garcia M O, Gurenko A A, Kamenetsky V S, Kerr A C, Krivolutskaya N A, Matvienkov V V, Nikogosian I K, Rocholl A, Sigurdsson I A, Sushchevskaya N M, Teklay M. 2007. The amount of recycled crust in sources of mantle-derived melts. *Science*, 316: 412–417.

Sobolev A V, Hofmann A W, Sobolev S V, Nikogosian I K. 2005. An olivine-free mantle source of Hawaiian shield basalts. *Nature*, 434(7033): 590–597.

Song X Y, Hua W Q, Hu R Z, Chen L M, Yu S Y. 2013. Formation of thick stratiform Fe-Ti oxide layers in layered intrusion and frequent replenishment of fractionated mafic magma: Evidence from the Panzhihua intrusion, SW China. *Geochemistry*, *Geophysics*, *Geosystems*, 14: 712–732.

Sorbadere F, Laurenz V, Frost D J, Wenz M, Rosenthal A, McCammon C, Rivard C. 2018. The behaviour of ferric iron during partial melting of peridotite. *Geochimica et Cosmochimica Acta*, 239: 235–254.

Tang Q Y, Ma Y S, Zhang M J, Li C S, Zhu D, Tao Y. 2013. Origin of Ni-Cu-PGE sulfide mineralization in the margin of the Zhubu mafic-ultramafic intrusion in the Emeishan Large Igneous Province, Southwestern China. *Economic Geology*, 108: 1889–1901.

Tao Y, Li C S, Hu R Z, Qi L, Qu W J, Du A D. 2010. Re-Os isotopic constraints on the genesis of the Limahe Ni-Cu deposit in the Emeishan large igneous province, SW China. *Lithos*, 119: 137–146.

Tao Y, Li C S, Hu R Z, Ripley E M, Du A D, Zhong H. 2007. Petrogenesis of the Pt-Pd mineralized Jinbaoshan ultramafic intrusion in the Permian Emeishan large igneous province, SW China. *Contributions to Mineralogy and Petrology*, 153(3): 321–337.

Tao Y, Li C S, Song X Y, Ripley E M. 2008. Mineralogical, petrological, and geochemical studies of the Limahe mafic-ultramatic intrusion and associated Ni-Cu sulfide ores, SW China. *Mineralium Deposita*, 43(8): 849–872.

Tao Y, Putirka K, Hu R Z, Li C S. 2015. The magma plumbing system of the Emeishan large igneous province and its role in basaltic magma differentiation in a continental setting. *American Mineralogist*, 100(11–12): 2509–2517.

Thompson R N, Gibson S A, Dickin A P, Smith P M. 2001. Early Cretaceous basalt and picrite dykes of the southern Etendeka region, NW Namibia: Windows into the role of the Tristan mantle plume in Paraná-Etendeka magmatism. *Journal of Petrology*, 42(11): 2049–2081.

Wan Z, Coogan L A, Canil D. 2008. Experimental calibration of aluminum partitioning between olivine and spinel as a geothermometer. *American Mineralogist*, 93(7): 1142–1147.

Wang C Y, Zhou M F. 2013. New textural and mineralogical constraints on the origin of the Hongge Fe-Ti-V oxide deposit, SW China. *Mineralium Deposita*, 48(6): 787–798.

Wang C Y, Zhou M F, Qi L. 2007. Permian flood basalts and mafic intrusions in the Jinping (SW China)-Song Da (northern Vietnam) district: Mantle sources, crustal contamination and sulfide segregation. *Chemical Geology*, 243(3–4): 317–343.

Wang C Y, Zhou M F, Qi L. 2010. Origin of extremely PGE-rich mafic magma system: An example from the Jinbaoshan ultramafic sill, Emeishan Large Igneous Province, SW China. *Lithos*, 119: 147–161.

Wang C Y, Zhou M F, Zhao Z D. 2005. Mineral chemistry of

chromite from the Permian Jinbaoshan Pt-Pd-sulphide-bearing ultramafic intrusion in SW China with petrogenetic implications. *Lithos*, 83(1): 47–66.

Wang C Y, Zhou M F, Zhao Z D. 2008. Fe-Ti-Cr oxides from the Permian Xinjie mafic-ultramafic layered intrusion in the Emeishan large igneous province, SW China: Crystallization from Fe- and Ti-rich basaltic magmas. *Lithos*, 102: 198–207.

Wignall P B, Sun Y D, Bond D P G, Izon G, Newton R J, Védrine S, Widdowson M, Ali R J, Lai X L, Jiang H S, Cope H, Bottrell S H. 2009. Volcanism, mass extinction, and carbon isotope fluctuations in the Middle Permian of China. *Science*, 324(5931): 1179–1182.

Wood B J, Bryndzia L T, Johnson K E. 1990. Mantle oxidation state and its relationship to tectonic environment and fluid speciation. *Science*, 248(4953): 337–345.

Wu Y D, Ren Z Y, Handler M R, Zhang L, Qian S P, Xu Y G, Wang C Y, Wang Y, Chen L L. 2018. Melt diversity and magmatic evolution in the Dali picrites, Emeishan Large Igneous Province. *Journal of Geophysical Research*: *Solid Earth*, 123(11): 9635–9657.

Xiao L, Xu Y G, Mei H J, Zheng Y F, He B, Pirajno F. 2004. Distinct mantle sources of low-Ti and high-Ti basalts from the western Emeishan large igneous province, SW China: Implications for plume-lithosphere interaction. *Earth and Planetary Science Letters*, 228(3): 525–546.

Xu J F, Suzuki K, Xu Y G, Mei H J, Li J. 2007. Os, Pb, and Nd isotope geochemistry of the Permian Emeishan continental flood basalts: Insights into the source of a large igneous province. *Geochimica et Cosmochimica Acta*, 71(8): 2104–2119.

Xu R, Liu Y S, Lambart S. 2020. Melting of a hydrous peridotite mantle source under the Emeishan large igneous province. *Earth-Science Reviews*, 207, 103253.

Xu Y C, Yang Z Y, Tong Y B, Jing X Q. 2018. Paleomagnetic secular variation constraints on the rapid eruption of the Emeishan continental flood basalts in southwestern China and northern Vietnam. *Journal of Geophysical Research*: *Solid Earth*, 123(4): 2597–2617.

Xu Y G, Chung S L, Jahn B M, Wu G Y. 2001. Petrologic and geochemical constraints on the petrogenesis of Permian-Triassic Emeishan flood basalts in southwestern China. *Lithos*, 58: 145–168.

Xu Y G, Chung S L, Shao H, He B. 2010. Silicic magmas from the Emeishan large igneous province, Southwest China: Petrogenesis and their link with the end-Guadalupian biological crisis. *Lithos*, 119(1–2): 47–60.

Xu Y G, He B, Chung S L, Menzies M A, Frey F A. 2004. Geologic, geochemical, and geophysical consequences of plume involvement in the Emeishan flood-basalt province. *Geology*, 32(10): 917–920.

Yang C, Liu S A. 2019. Zinc isotope constraints on recycled oceanic crust in the mantle sources of the Emeishan large igneous province. *Journal of Geophysical Research*: *Solid Earth*, 124(22), 12537–12555.

Yang J, Cawood P A, Du Y S. 2015. Voluminous silicic eruptions during late Permian Emeishan igneous province and link to climate cooling. *Earth and Planetary Science Letters*, 432: 166–175.

Yang Z F, Li J, Liang W F, Luo Z H. 2016. On the chemical markers of pyroxenite contributions in continental basalts in Eastern China: Implications for source lithology and the origin of basalts. *Earth-Science Reviews*, 157: 18–31.

Yao J H, Zhu W G, Li C, Zhong H, Yu S, Ripley E M, Bai Z J. 2019. Olivine O isotope and trace element constraints on source variation of picrites in the Emeishan flood basalt province, SW China. *Lithos*, 338: 87–98.

Yu S Y, Chen L M, Lan J B, He Y S, Chen Q, Song X Y. 2020. Controls of mantle source and condition of melt extraction on generation of the picritic lavas from the Emeishan large igneous province, SW China. *Journal of Asian Earth Sciences*, 203, 104534.

Yu S Y, Shen N P, Song X Y, Ripley E M, Li C, Chen L M. 2017. An integrated chemical and oxygen isotopic study of primitive olivine grains in picrites from the Emeishan Large Igneous Province, SW China: Evidence for oxygen isotope heterogeneity in mantle sources. *Geochimica et Cosmochimica Acta*, 215: 263–276.

Yu S Y, Song X Y, Chen L M, Li X B. 2014. Postdated melting of subcontinental lithospheric mantle by the Emeishan mantle plume: Evidence from the Anyi intrusion, Yunnan, SW China. *Ore Geology Reviews*, 57: 560–573.

Zhang L, Ren Z Y, Handler M R, Wu Y D, Zhang L, Qian S P, Xia X P, Yang Q, Xu Y G. 2019a. The origins of high-Ti and low-Ti magmas in large igneous provinces, insights from melt inclusion trace elements and Sr-Pb isotopes in the Emeishan large Igneous Province. *Lithos*, 344: 122–133.

Zhang L, Ren Z Y, Xia X P, Yang Q, Hong L B, Wu D. 2019b. *In situ* determination of trace elements in melt inclusions using laser ablation-inductively coupled plasma-sector field-mass spectrometry. *Rapid Communications*

in Mass Spectrometry, 33(4): 361–370.

Zhang L, Ren Z Y, Zhang L, Wu Y D, Qian S P, Xia X P, Xu Y G. 2021. Nature of the mantle plume under the Emeishan large igneous province: Constraints from olivine-hosted melt inclusions of the Lijiang picrites. *Journal of Geophysical Research*: *Solid Earth*, 126(5), e2020JB021022.

Zhang Y, Ren Z Y, Xu Y G. 2013. Sulfur in olivine-hosted melt inclusions from the Emeishan picrites: Implications for S degassing and its impact on environment. *Journal of Geophysical Research*: *Solid Earth*, 118(18): 4063–4070.

Zhang Z C, Mahoney J J, Mao J W, Wang F S. 2006. Geochemistry of picritic and associated basalt flows of the western Emeishan flood basalt province, China. *Journal of Petrology*, 47(10): 1997–2019.

Zhang Z C, Zhi X C, Chen L, Saunders A D, Reichow M K. 2008. Re-Os isotopic compositions of picrites from the Emeishan flood basalt province, China. *Earth and Planetary Science Letters*, 276(1–2): 30–39.

Zhong H, Qi L, Hu R Z, Zhou M F, Gou T Z, Zhu W G, Liu B G, Zhu Y C. 2011. Rhenium-osmium isotope and platinum-group elements in the Xinjie layered intrusion, SW China: Implications for source mantle composition, mantle evolution, PGE fractionation and mineralization. *Geochimica et Cosmochimica Acta*, 75(6): 1621–1641.

Zhong Y T, He B, Mundil R, Xu Y G. 2014. CA-TIMS zircon U-Pb dating of felsic ignimbrite from the Binchuan section: Implications for the termination age of Emeishan large igneous province. *Lithos*, 204: 14–19.

Zhong Y T, Mundil R, Chen J, Yuan D X, Denyszyn S W, Jost A B, Payne J L, He B, Shen S J, Xu Y G. 2020. Geochemical, biostratigraphic, and high-resolution geochronological constraints on the waning stage of Emeishan Large Igneous Province. *Geological Society of America Bulletin*, 132(9–10): 1969–1986.

Zhou M F, Arndt N T, Malpas J, Wang C Y, Kennedy A K. 2008. Two magma series and associated ore deposit types in the Permian Emeishan large igneous province, SW China. *Lithos*, 103(3–4): 352–368.

Zhou M F, Zhao J H, Qi L, Su W C, Hu R Z. 2006. Zircon U-Pb geochronology and elemental and Sr-Nd isotope geochemistry of Permian mafic rocks in the Funing area, SW China. *Contributions to Mineralogy and Petrology*, 151(1): 1–19.

The Nature of Mantle Source of the Pingchuan Picrites in the Emeishan Large Igneous Province — Constrains from the Trace Element Composition of Olivines

ZHANG Lei[1, 2, 3], REN Zhongyuan[1, 2*], ZHANG Le[1, 2]

(1. *State Key Laboratory of Isotope Geochemistry*, *Guangzhou Institute of Geochemistry*, *Chinese Academy of Sciences*, *Guangzhou* 510640, *Guangdong*, *China;* 2. *CAS Center for Excellence in Deep Earth Science*, *Guangzhou* 510640, *Guangdong*, *China*; 3. *University of Chinese Academy of Sciences*, *Beijing* 100049, *China*)

Abstract: Olivine is one of the earliest crystallized silicates from basaltic magmas. The major and trace element compositions of olivine phenocrysts can provide important information about the thermodynamic condition of the magma, source lithology, and source component, including the nature of the recycled component. The major and trace element compositions of the olivines and Cr-spinel inclusions in the olivines from the Pingchuan picrites in the Emeishan large igneous province were analyzed in this study, and compared with the compositions of the olivines and spinels in the Dali picrites, and the differences of source component and oxygen fugacity of parental magmas of different picrites were discussed. The Pingchuan olivines have higher V/Sc ratio than the Dali olivines, which indicates a more oxidized condition for the Pingchuan magma. The olivine-spinel oxybarometer shows that the $\log f_{O_2}$ values of the Pingchuan and the Dali magmas, which are saturated with olivine and spinel, are ΔQFM+0.24 and ΔQFM−0.51, respectively. The high Fo olivines in the Pingchuan picrites have Ni/Co>20, which implies the presence of recycled component in the source of the Pingchuan picrites. The lower Li content of the Pingchuan olivines indicates that the component that recycled into the source is oceanic crust. In the mantle source discrimination diagrams of olivine Ni *vs.* Mn/Zn and 100×Mn/Fe *vs.* 10000×Zn/Fe, the Pingchuan olivines are mainly plotted within the fields of peridotite sources. However, the Pingchuan olivines exhibit higher Ni, Co, Zn/Fe, Fe/Mn, and lower Ca, Mn, Sc, Mn/Zn than the Dali olivines, which suggest the presence of pyroxenite component in the source of the Pingchuan picrites. A small amount of recycled oceanic crust adding into the mantle peridotite would produce an olivine relatively enriched sources. The olivines crystallized from melts derived from such a mantle source would have characteristics similar to the olivines from the Pingchuan picrites, which still have compositions similar to the olivines crystallized from a peridotite partial melting melts. However, the compositions of the olivines in the Pingchuan picrites are also controlled by the pyroxenite component in the source. Combined with the wide compositional ranges of the olivines, we suggest that the Pingchuan picrites were derived from a source containing pyroxenite components rather than a homogeneous peridotite source.

Keywords: Emeishan large igneous province; picrite; olivine; pyroxenite; oxygen fugacity